

Spin asymmetries A_1 and structure functions g_1 of the proton and the deuteron from polarized high energy muon scattering

B. Adeva,¹⁸ T. Akdogan,² E. Arik,² A. Arvidson,^{21,a} B. Badelek,^{21,23} G. Bardin,^{17,b} G. Baum,¹ P. Berglund,⁸ L. Betev,¹³ I. G. Bird,^{17,ff} R. Birsas,²⁰ P. Björkholm,^{21,c} N. de Botton,¹⁷ M. Boutemur,^{24,d} F. Bradamante,²⁰ A. Bravar,¹¹ A. Bressan,^{20,e} S. Bültmann,^{1,f} E. Burtin,¹⁷ C. Cavata,¹⁷ D. Crabb,²² J. Cranshaw,²⁰ T. Çuhadar,^{2,15} S. Dalla Torre,²⁰ R. van Dantzig,¹⁵ B. Derro,⁴ A. Deshpande,²⁴ S. Dhawan,²⁴ C. Dulya,^{15,4,g} A. Dyring,²¹ S. Eichblatt,^h J. C. Faivre,¹⁷ D. Fasching,^{16,i} F. Feinstein,¹⁷ C. Fernandez,^{18,9} S. Forthmann,⁷ B. Frois,¹⁷ A. Gallas,¹⁸ J. A. Garzon,^{18,9} H. Gilly,⁶ M. Giorgi,²⁰ E. von Goeler,^j S. Goertz,³ I. A. Golutvin,¹⁰ G. Gracia,^{18,k} N. de Groot,^{15,l} M. Grosse Perdekamp,^{24,m} K. Haft,¹³ D. von Harrach,¹¹ T. Hasegawa,^{14,n} P. Hautle,^{5,o} N. Hayashi,^{14,p} C. A. Heusch,^{5,q} N. Horikawa,¹⁴ V. W. Hughes,²⁴ G. Igo,⁴ S. Ishimoto,^{14,r} T. Iwata,¹⁴ E. M. Kabuß,¹¹ T. Kageya,^{14,s} A. Karev,¹⁰ H. J. Kessler,^{6,t} T. J. Ketel,¹⁵ J. Kiryluk,²³ I. Kiryushin,¹⁰ A. Kishi,¹⁴ Yu. Kisselev,¹⁰ L. Klostermann,¹⁵ D. Krämer,¹ V. Krivokhijine,¹⁰ W. Kröger,^{5,q} V. Kukhtin,¹⁰ K. Kurek,²³ J. Kyyräinen,^{1,8} M. Lamanna,²⁰ U. Landgraf,⁶ J. M. Le Goff,¹⁷ F. Lehar,¹⁷ A. de Lesquen,¹⁷ J. Lichtenstadt,¹⁹ T. Lindqvist,²¹ M. Litmaath,^{15,e} M. Lowe,^u A. Magnon,¹⁷ G. K. Mallot,^{11,e} F. Marie,¹⁷ A. Martin,²⁰ J. Martino,¹⁷ T. Matsuda,^{14,n} B. Mayes,⁹ J. S. McCarthy,²² K. Medved,¹⁰ W. Meyer,³ G. van Middelkoop,¹⁵ D. Miller,¹⁶ Y. Miyachi,¹⁴ K. Mori,¹⁴ J. Moromisato,^j A. Nagaitsev,¹⁰ J. Nassalski,²³ L. Naumann,^{5,b} T. O. Niinikoski,⁵ J. E. J. Oberski,¹⁵ A. Ogawa,^{14,v} C. Ozben,² H. Pereira,¹⁷ F. Perrot-Kunne,¹⁷ D. Peshekhonov,¹⁰ R. Piegia,^{5,w} L. Pinsky,⁹ S. Platchkov,¹⁷ M. Plo,¹⁸ D. Pose,¹⁰ H. Postma,¹⁵ J. Pretz,^{11,x} R. Puntaferro,²⁰ T. Pussieux,¹⁷ G. Rädcl,⁵ A. Rijllart,⁵ G. Reicherz,³ J. Roberts,⁹ S. Rock,^{5,y} M. Rodriguez,^{21,w} E. Rondio,^{23,5} L. Ropelewski,^{23,e} I. Sabo,¹⁹ J. Saborido,^{18,e} A. Sandacz,²³ I. Savin,¹⁰ P. Schiavon,²⁰ A. Schiller,⁷ K. P. Schüler,^{24,z} R. Seitz,^{11,aa} Y. Semertzidis,^{5,bb} S. Sergeev,¹⁰ P. Shanahan,^{16,h} E. P. Sichtermann,¹⁵ F. Simeoni,²⁰ G. I. Smirnov,¹⁰ A. Staude,¹³ A. Steinmetz,^{11,13} U. Stiegler,⁵ H. Stuhmann,⁷ M. Szeleper,²³ F. Tassarotto,²⁰ D. Thers,¹⁷ W. Tlaczala,^{23,cc} A. Tripet,¹ G. Unel,² M. Velasco,^{16,e} J. Vogt,¹³ R. Voss,⁵ C. Whitten,⁴ R. Windmolders,¹² R. Willumeit,⁷ W. Wislicki,²³ A. Witzmann,^{6,dd} J. Ylöstalo,⁸ A. M. Zanetti,²⁰ K. Zaremba,^{23,cc} N. I. Zamiatin,¹⁰ and J. Zhao^{7,ee}

(Spin Muon Collaboration)

¹University of Bielefeld, Physics Department, D-33501 Bielefeld, Germany

²Bogaziçi University and Istanbul Technical University, Istanbul, Turkey

³University of Bochum, Physics Department, D-44780 Bochum, Germany

⁴University of California, Department of Physics, Los Angeles, California 90024

⁵CERN, 1211 Geneva 23, Switzerland

⁶University of Freiburg, Physics Department, D-79104 Freiburg, Germany

⁷GKSS, D-21494 Geesthacht, Germany

⁸Helsinki University of Technology, Low Temperature Laboratory and Institute of Particle Physics Technology, Espoo, Finland

⁹University of Houston, Department of Physics, Houston, Texas 77204-5506

¹⁰JINR, Dubna, RU-141980 Dubna, Russia

¹¹University of Mainz, Institute for Nuclear Physics, D-55099 Mainz, Germany

¹²University of Mons, Faculty of Science, 7000 Mons, Belgium

¹³University of Munich, Physics Department, D-80799 Munich, Germany

¹⁴Nagoya University, CIRSE and Department of Physics, Furo-Cho, Chikusa-Ku, 464 Nagoya, Japan

¹⁵NIKHEF, Delft University of Technology, FOM and Free University, 1009 AJ Amsterdam, The Netherlands

¹⁶Northwestern University, Department of Physics, Evanston, Illinois 60208

¹⁷CEA Saclay, DAPNIA, 91191 Gif-sur-Yvette, France

¹⁸University of Santiago, Department of Particle Physics, 15706 Santiago de Compostela, Spain

¹⁹Tel Aviv University, School of Physics, 69978 Tel Aviv, Israel

²⁰INFN Trieste and University of Trieste, Department of Physics, 34127 Trieste, Italy

²¹Uppsala University, Department of Radiation Sciences, 75121 Uppsala, Sweden

²²University of Virginia, Department of Physics, Charlottesville, Virginia 22901

²³Soltan Institute for Nuclear Studies and Warsaw University, 00681 Warsaw, Poland

²⁴Yale University, Department of Physics, New Haven, Connecticut 06511

(Received 18 May 1998; published 19 October 1998)

We present the final results of the spin asymmetries A_1 and the spin structure functions g_1 of the proton and the deuteron in the kinematic range $0.0008 < x < 0.7$ and $0.2 < Q^2 < 100 \text{ GeV}^2$. For the determination of A_1 , in addition to the usual method which employs inclusive scattering events and includes a large radiative background at low x , we use a new method which minimizes the radiative background by selecting events with at least one hadron as well as a muon in the final state. We find that this hadron method gives smaller errors for $x < 0.02$, so it is combined with the usual method to provide the optimal set of results.

[S0556-2821(98)07017-9]

PACS number(s): 13.60.Hb, 13.88.+e

I. INTRODUCTION

Polarized deep inelastic lepton-nucleon scattering is an important tool to study the spin structure of the nucleon. Measurements with proton, deuteron, and helium-3 targets have determined the spin structure functions of the nucleon and have verified the Bjorken sum rule [1], which is a fundamental relation of QCD.

In the last five years, the Spin Muon Collaboration (SMC) at CERN has reported experimental results on the spin structure of the proton [2–8] and of the deuteron [3,5,8–11], measured in inelastic muon scattering at beam energies of 100 and 190 GeV. Thus far our published results for the virtual photon-proton and virtual photon-deuteron cross section asymmetries $A_1^p(x, Q^2)$ and $A_1^d(x, Q^2)$ and for the spin-dependent structure functions $g_1^p(x, Q^2)$ and $g_1^d(x, Q^2)$ have been obtained from inclusive scattering events. These results are updated in this paper, principally with a final value for the muon beam polarization.

Since the inclusive scattering events include a large radiative background at low x , we now employ a new and alter-

native method of determining the asymmetries which requires at least one hadron as well as a muon in the final state. This hadron method removes the background due to elastic and quasielastic scattering accompanied by a high energy bremsstrahlung photon, and improves the statistical accuracy of the measurement at low x . A similar method has been applied successfully by the New Muon Collaboration (NMC) [12] and the E665 [13] analyses of F_2 structure function ratios.

Our final results for the asymmetries A_1^p and A_1^d are based on both the inclusive and the hadron methods and cover the kinematic region of $0.0008 < x < 0.7$ and $Q^2 > 0.2 \text{ GeV}^2$. An optimal set is defined with the inclusive method being used for $x > 0.02$ and the hadron method for $x < 0.02$. In the low x region the statistical errors from the hadron method are smaller than those from the inclusive method. The range of reduction varies from 1 to 0.6 with decreasing x . For $Q^2 > 1 \text{ GeV}^2$ the lowest x reached is 0.003 where the reduction factor is 0.8. Results presented here stem from 15.6 and 19.0 million events accepted after all cuts for the A_1^p and the A_1^d determinations, respectively.

The outline of this paper is as follows. Section II gives the formulae for the asymmetry determination and explains the update of the beam polarization, while Sec. III describes in detail the hadron method. In Sec. IV, after showing the updated result for the A_1 measurement with the inclusive method, we give the results for the hadron method, compare both, and finally define the optimal data set by using the hadron method at low x and the inclusive one at high x . Section V presents the structure functions g_1 and Sec. VI their integrals in the measured x range as well as their first moments with contributions from the unmeasured region taken from the QCD analysis (see our following paper [14]). In Sec. VII we calculate the nonsinglet combination $g_1^p - g_1^n$, compare it to the corresponding unpolarized combination $F_1^p - F_1^n$, and compute its integral in the measured range and its first moment. Section VIII contains a summary. The detailed discussion of the first moments $\Gamma_1^{p,d}$ and the Bjorken sum rule is presented in our following paper [14]. The Appendix gives a parametrization of the world data on the spin

^aNow at The Royal Library, 102 41 Stockholm, Sweden.

^bDeceased.

^cNow at Ericsson Infotech AB, Karlstad, Sweden.

^dNow at University of Munich, Physics Department, D-80799 Munich, Germany.

^eNow at CERN, 1211 Geneva 23, Switzerland.

^fNow at University of Virginia, Department of Physics, Charlottesville, VA 22901.

^gNow at CIEMAT, Avda Complutense 22, 28040, Madrid, Spain.

^hNow at Fermi National Accelerator Laboratory, Batavia, IL 60510.

ⁱNow at University of Wisconsin.

^jPermanent address: Northeastern University, Department of Physics, Boston, MA 02115.

^kNow at NIKHEF P.O.B. 41882, 1009 DB Amsterdam, The Netherlands.

^lNow at SLAC, Stanford CA 94309.

^mNow at University of Mainz, Institute of Nuclear Physics, D-55099, Germany.

ⁿPermanent address: Miyazaki University, Faculty of Engineering, 889-21 Miyazaki-Shi, Japan.

^oPermanent address: Paul Scherrer Institut, 5232 Villigen, Switzerland.

^pPermanent address: The Institute of Physical and Chemical Research (RIKEN), Wako 351-01, Japan.

^qPermanent address: University of California, Institute of Particle Physics, Santa Cruz, CA 95064.

^rPermanent address: KEK, Tsukuba-Shi, 305 Ibaraki-Ken, Japan.

^sNow at University of Michigan, Ann Arbor MI 48109.

^tNow at SBC Warburg Dillon Read, CH-4002 Basel, Switzerland.

^uPermanent address: Rice University, Bonner Laboratory, Houston, TX 77251-1892.

^vNow at Penn. State University, 303 Osmond Lab, University Park, PA 16802.

^wPermanent address: University of Buenos Aires, Physics Department, 1428 Buenos Aires, Argentina.

^xNow at Physics Department, Yale University, New Haven, CT 06520.

^yPermanent address: The American University, Washington D.C. 20016.

^zNow at DESY, Notkestrasse 85, Hamburg, Germany.

^{aa}Now at Université de Montréal, Montréal, PQ, H3C 3J7, Canada.

^{bb}Permanent address: Brookhaven National Laboratory, Upton, NY 11973.

^{cc}Permanent address: Warsaw University of Technology, Warsaw, Poland.

^{dd}Now at F. Hoffmann-La Roche Ltd., CH-4070 Basel, Switzerland.

^{ee}Now at Los Alamos National Laboratory, Los Alamos, NM 87545.

^{ff}Now at Jefferson Laboratory, Newport News, VA.

TABLE I. Main characteristics of different measurements in the SMC experiment: beam energy, target material, and average target polarization with the relative accuracy of its measurement. The last column refers to publications concerning the experiments.

| Year | Beam energy (GeV) | Target | Target polarization | | References |
|------|-------------------|----------------------------------|-----------------------|------------------------|---------------|
| | | | $\langle P_t \rangle$ | $\Delta P_t / P_t$ (%) | |
| 1992 | 100 | C ₄ D ₉ OD | 0.40 | ± 5 | [9,5,8,11] |
| 1993 | 190 | C ₄ H ₉ OH | 0.86 | ± 3.0 | [2,4,6,7,5,8] |
| 1994 | 190 | C ₄ D ₉ OD | 0.49 | ± 5.4 | [10,11,5,8] |
| 1995 | 190 | C ₄ D ₉ OD | 0.50 | ± 2.1 | [11,8] |
| 1996 | 190 | NH ₃ | 0.89 | ± 2.7 | [7,8] |

independent structure functions $F_2^{p,d}$ which we used in the analysis.

II. ASYMMETRY DETERMINATION

The experimental setup and the data taking procedure are described elsewhere [6]. Evaluation of the cross section asymmetries for parallel and antiparallel configurations of longitudinal beam and target polarizations

$$A_{\parallel} = \frac{\sigma^{\uparrow\downarrow} - \sigma^{\uparrow\uparrow}}{\sigma^{\uparrow\downarrow} + \sigma^{\uparrow\uparrow}}, \quad (1)$$

from the measured counting rate asymmetry $A_{\parallel}^{\text{meas}}$ requires knowledge of the incident muon and target nucleon polarizations P_{μ} and P_t and of the dilution factor f which accounts for the fact that only a fraction of the target nucleons is polarizable ($A_{\parallel}^{\text{meas}} = f P_t P_{\mu} A_{\parallel}$).

The beam polarization was determined in a dedicated setup, by measuring the cross section asymmetry for the scattering of polarized beam muons from longitudinally polarized atomic electrons [6,15] and, independently, by measuring the energy spectrum of the positrons originating from muon decays [16,17]. The former method results in $P_{\mu} = -0.788 \pm 0.023$ and the latter in $P_{\mu} = -0.806 \pm 0.029$, which are combined to give

$$P_{\mu} = -0.795 \pm 0.019 \quad (2)$$

for an average muon energy of 187.4 GeV. The analysis of the decay method has been improved, and for both methods the results are statistically compatible with results obtained before with only part of the data [7,16]. The muon beam is not monochromatic and the polarization depends on the energy. The polarization used in our previous publications [7,11] is equivalent to $P_{\mu} = -0.763 \pm 0.03$ for an average energy of 187.4 GeV. The relative change of 4% in P_{μ} with respect to Eq. (2) will directly reflect in the asymmetry. The beam polarization for the small part of the data obtained at lower beam energy, $P_{\mu} = -0.81 \pm 0.03$ for an average beam energy of 99.4 GeV, is the same as before.

The various target materials and the typical proton or deuteron polarizations are listed in Table I. A detailed description of the target setup can be found in Refs. [6, 18].

The asymmetries $A_{\parallel}^{p,d}$ and the spin-dependent structure functions $g_1^{p,d}$ are related to the virtual photon-proton (deuteron) asymmetries $A_1^{p,d}$ and $A_2^{p,d}$ [19,20] by

$$A_{\parallel}^{p,d} = D(A_1^{p,d} + \eta A_2^{p,d}),$$

$$g_1^{p,d} = \frac{F_2^{p,d}}{2x(1+R)} (A_1^{p,d} + \gamma A_2^{p,d}), \quad (3)$$

where the factors η and γ depend only on kinematic variables. The depolarization factor D depends in addition on the ratio of the photoabsorption cross sections for longitudinally and transversely polarized virtual photons $R = \sigma_L / \sigma_T$. The virtual photon-proton asymmetries are defined as

$$A_1^p = \frac{\sigma_{1/2} - \sigma_{3/2}}{\sigma_{1/2} + \sigma_{3/2}}, \quad A_2^p = \frac{2\sigma^{TL}}{\sigma_{1/2} + \sigma_{3/2}}, \quad (4)$$

where $\sigma_{1/2}$ ($\sigma_{3/2}$) is the photoabsorption cross section of a transversely polarized virtual photon by a proton, with total spin projection $\frac{1}{2}$ ($\frac{3}{2}$) in the photon direction and σ^{TL} is a term arising from the interference between transverse and longitudinal amplitudes. For more details regarding the kinematic factors η , γ , and D the reader is referred to Ref. [6]. Corresponding formulas for the deuteron are

$$A_1^d = \frac{1}{2} (\sigma_0^T - \sigma_2^T) / \sigma_T,$$

$$A_2^d = \frac{1}{2} (\sigma_0^{TL} + \sigma_1^{TL}) / \sigma_T. \quad (5)$$

Here $\sigma_T = \frac{1}{3} (\sigma_0^T + \sigma_1^T + \sigma_2^T)$ is the transverse photoabsorption cross section, σ_J^T is the cross section for absorption of a virtual photon by a deuteron with total spin projection J in the photon direction, and σ_J^{TL} results from the interference between transverse and longitudinal amplitudes for $J=0,1$.

In the kinematic region of our measurement η and γ are small. The asymmetries A_2^p and A_2^d were measured and found to be consistent with zero [4,11,21]. For these reasons we neglect the A_2 terms in Eq. (3) and estimate the systematic uncertainty in A_1 due to a possible contribution of A_2 [7,11].

III. THE HADRON METHOD

A. Description of the procedure

In previous publications the determination of A_1 from SMC data was done using an inclusive event selection, requiring only a scattered muon. In addition to deep inelastic scattering events, the resulting sample includes scattering events which are elastic on free target nucleons, or elastic or quasielastic on target nuclei and which are accompanied by the radiation of a hard photon. These radiative events do not carry any information on the spin structure of the nucleon and only degrade the statistical accuracy of the measurement. Elastic μ - e interactions also do not carry any information on the nucleon spin; they are peaked at $x = m_e / m_p \approx 0.0005$ and give for $x > 0.0008$ only a small contribution, which is not

considered in the following discussion. The described radiative events dilute the spin effects in the cross section for the inclusive sample, similarly to the nonpolarizable nuclei in the target, accounted for by the dilution factor f . The effective dilution factor f' ,

$$f' = \frac{\sigma_{1\gamma}^{p,d}}{\sigma_{\text{tot}}^{p,d}} f = \frac{n_{p,d} \sigma_{1\gamma}^{p,d}}{\sum_A n_A \sigma_{\text{tot}}^A}, \quad (6)$$

accounts for both diluting sources. The sum runs over all types of target nuclei. Essentially only protons or deuterons are polarized in the target. For the description of a small correction to the asymmetry due to the polarized background of ^{14}N for the NH_3 target and of protons for the deuterated butanol target, see Refs. [2, 7]. The total cross section σ_{tot} and the one-photon-exchange (Born) cross section $\sigma_{1\gamma}$ are related by $\sigma_{\text{tot}} = \lambda \sigma_{1\gamma} + \sigma_{\text{tail}}^{\text{el}} + \sigma_{\text{tail}}^{\text{qel}} + \sigma_{\text{tail}}^{\text{inel}}$, where the σ_{tail} terms are the cross sections from the radiative tails (elastic, quasi-elastic, and inelastic reactions). The factor λ , which does not depend on the polarization, corrects for higher order contributions: virtual (vacuum and vertex corrections) and soft real photon radiation [6]. For an effective measurement the dilution factor f' should be large.

In the new method of analyzing the data we use only events for which at least one hadron track has been reconstructed; then these *hadron-tagged events* do not include any contribution from $\sigma_{\text{tail}}^{\text{el}}$ and $\sigma_{\text{tail}}^{\text{qel}}$ since the recoil proton can not be observed in our spectrometer due to its small energy. The total cross section for hadron-tagged events thus reduces to

$$\sigma_{\text{tot}}^{\text{tagged}} = \lambda \sigma_{1\gamma} + \sigma_{\text{tail}}^{\text{inel}}. \quad (7)$$

In the calculation of the effective dilution factor f' for hadron-tagged events, $\sigma_{\text{tot}}^{\text{tagged}}$ replaces σ_{tot} in Eq. (6) and the effective dilution factor increases accordingly,¹ in particular at low x , as can be seen in Fig. 1.

The fraction of deep inelastic events which would not be selected as hadron-tagged events with $Q^2 > 1 \text{ GeV}^2$ for our spectrometer was estimated by a Monte Carlo simulation to be in the range of 2–7 % for $x < 0.02$ and to increase at higher x . This loss of events worsens the statistical accuracy only with a square root dependence while the increase in the dilution factor improves it linearly. The result is that the hadron method gives a net gain in statistical accuracy for $x < 0.02$.

B. Event selection

As for the inclusive method, events have to satisfy the following kinematic cuts: energy of the scattered muon $E'_\mu > 19 \text{ GeV}$, $\nu = E_\mu - E'_\mu > 15 \text{ GeV}$, $y = \nu/E_\mu < 0.9$, and scattering angle $\theta > 2 \text{ mrad}$. Events are then labeled inelastic when at least one hadron is found in the final state. As only

¹Actually the contribution from $\sigma_{\text{tail}}^{\text{inel}}$ is also reduced by the requirement that a hadron above a certain energy threshold has to be produced. The estimate of this reduction is included only in the systematic error.

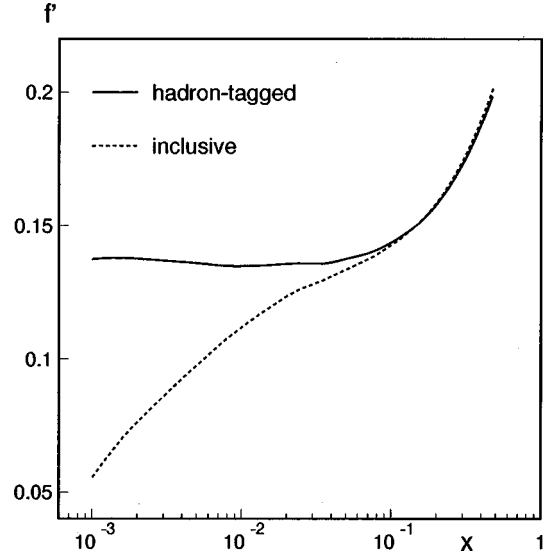


FIG. 1. Effective dilution factor f' for hadron tagged and for inclusive events from the ammonia target.

tracks of charged particles are reconstructed in our spectrometer we can observe neutral hadrons indirectly via their charged decay products, or in the case of a π^0 meson through converted photons from its decay.

For hadron-tagged events we require, in addition to a scattered muon either one or more tracks pointing to the muon interaction vertex, or a pair of tracks with positive and negative charge from a secondary vertex. The sample, selected in this way, still contains some unwanted radiative events in which the bremsstrahlung photon is converted. These unwanted events occur at large y and at a small angle α between the direction of the produced particle and the direction of the muon momentum loss $\vec{p}_\mu - \vec{p}'_\mu$, which for radiative elastic and quasielastic events is very close to the direction of the bremsstrahlung photon. An enhancement of events at small α and large y is indeed seen in the data; it disappears if a signature for a charged hadron is required in the calorimeter [22]. Also, such an enhancement is not present in a Monte Carlo simulation which includes only deep inelastic scattering (DIS) events. To remove these radiative events from the sample, but not events with π^0 mesons, additional conditions were applied: to keep an event we require that tracks, giving a calorimeter response compatible with that for electrons, have $\alpha > 4 \text{ mrad}$ or belong to an event with $y < 0.6$. The same is required for a pair of tracks from a secondary vertex compatible with photon conversion. The events surviving all of these cuts define the sample of hadron-tagged events.

C. Tests of the procedure

As a first test of the procedure of asymmetry extraction with hadron tagging the fraction of inclusive events selected as hadron-tagged events is compared with the expected one. The latter is calculated from the ratio of the corresponding effective dilution factors and the probability of detecting at least one hadron in DIS events. This probability was estimated with the Monte Carlo simulation mentioned before.

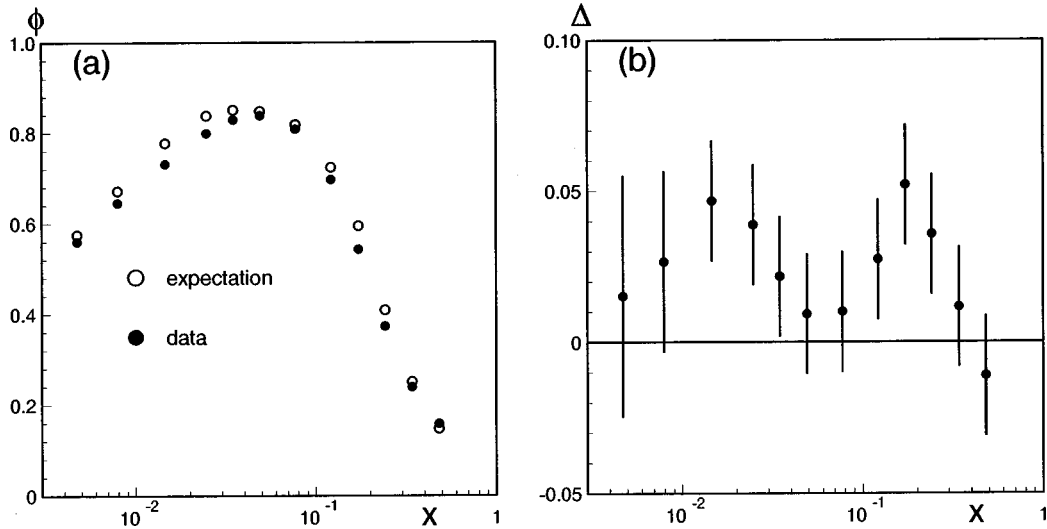


FIG. 2. (a) Fraction ϕ of the inclusive events selected as hadron tagged observed in the data, for the ammonia target, compared with the expectation (see text). (b) Difference Δ of the two fractions. Errors show the systematic uncertainty of the expected fraction of hadron-tagged events.

The comparison is presented in Fig. 2 for events with $Q^2 > 1 \text{ GeV}^2$ for which the fragmentation into hadrons is reliably described in the simulation. In the case of inefficient removal of radiative events, the fraction of inclusive events selected as hadron-tagged events would be larger than expected. Figure 2 shows that this is not the case.

The sensitivity of the measured asymmetry to the selection with tagging was checked by varying the tagging criteria as follows: keeping only tracks giving a good vertex fit, removing all tracks with an energy deposit in the calorimeter consistent with that expected for an electron, applying the cut on α to all tracks, or changing this cut from 4 to 2 mrad. The resulting differences in the asymmetries are compatible with zero for all x bins. For $x < 0.02$, where we will apply hadron tagging (see Sec. IV), the corresponding χ^2 probabilities are in the range of 5–70 % for the proton and 30–89 % for the deuteron.

Possible biases on A_1 introduced by hadron-tagging were also studied with a dedicated Monte Carlo simulation for $Q^2 > 1 \text{ GeV}^2$. The program POLDIS [23] was used to generate events, and the spectrometer acceptance for hadrons was approximated by requiring forward produced hadrons with momentum $p_h > 5 \text{ GeV}$ and $z = E_h/\nu > 0.1$, where E_h is the hadron energy. The asymmetries were calculated for events with such hadrons and compared to those obtained for all events. The differences are shown as a function of x in Fig. 3 for the proton and the deuteron. For the proton, the asymmetries calculated from hadron-tagged events are larger at high x . This is to be expected because in this region of x the total energy of the hadronic final state W is not very high and the observed hadron is most likely to be the leading one. Since the detection efficiency for charged hadrons, which are more abundant in u -quark than in d -quark fragmentation, is higher than for neutral hadrons, the hadron-tagged sample is enriched with scattering on u quarks compared to the inclusive sample. From semi-inclusive measurements [8] it is known that the polarization of the valence u quarks is positive

whereas that of the valence d quarks is negative. Therefore, one expects higher values of A_1 for the hadron-tagged event sample. If the hadron selection is relaxed ($z > 0.05$ and $p_h > 3 \text{ GeV}$) more nonleading hadrons are accepted and the asymmetry gets closer to the one for inclusive events, as can be seen in Fig. 3. At low x the available energy is large and the tagging no longer favors scattering on u quarks. The asymmetries for hadron-tagged and inclusive events should therefore be the same. Indeed, in this region the estimated differences are negligibly small. For the deuteron the effect of hadron tagging on A_1 is very small, as can be seen in Fig. 3. This is expected from isospin invariance. The hadron method is applied to the data at low x , also for $Q^2 < 1 \text{ GeV}^2$, where we do not expect a bias since W is large.

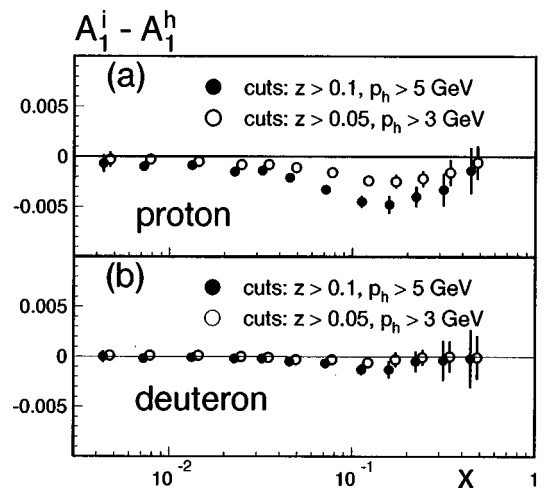


FIG. 3. The differences of $A_1^i - A_1^h$ calculated from Monte Carlo for all generated DIS events (A_1^i) and for events with at least one forward hadron surviving cuts on z and on the hadron momentum (A_1^h). The results are shown for two sets of cuts for the proton and for the deuteron.

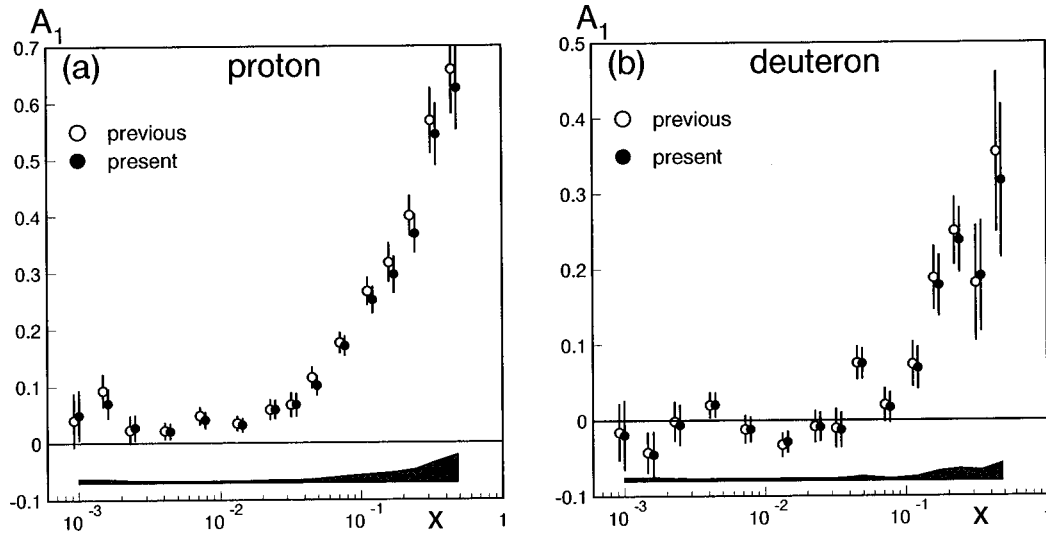


FIG. 4. The values of A_1 for (a) proton and (b) deuteron, updated as discussed in the text, in comparison with previously published results of Refs. [7] and [11]. Statistical errors are shown as error bars, while the shaded bands below indicate the systematic uncertainty.

IV. RESULTS FOR A_1 ASYMMETRIES

A. Updated A_1 with inclusive event selection

We have updated our previously published results on A_1 [7,11] for the proton and the deuteron using the new value of the beam polarization, given in Eq. (2). This leads to a 4% reduction of the A_1 values compared to the previous ones. In addition, there were other improvements which are discussed below.

The proton data collected in 1993 have been reprocessed with several improvements introduced since the original analysis. The most important was that information from an additional tracking chamber placed inside the spectrometer magnet just prior to the 1993 run was included in the track reconstruction. Also, the small angle triggers were treated in an improved way in the reconstruction. These changes,

among others, resulted in a gain of approximately 10% in the number of events, mainly at low x . The new combined proton asymmetries are shown in Fig. 4(a) along with the values from our previous publication [7].

The updated result for A_1 of the deuteron has been obtained using a new parametrization for F_2^d obtained in a similar way as the parametrization for F_2^p used in Ref. [7]. These F_2 fits are described in the Appendix. The parametrization for R used for $x < 0.12$ is based on recently published NMC [24] data, while for $x > 0.12$ we use the R parametrization from SLAC [25], as before. The new values of R change the depolarization factor at low x , while F_2^d and R enter in the effective dilution factor and also in the polarized radiative corrections. The overall effect of these changes is small. Figure 4(b) presents the updated results compared with the results from our previous publication [11].

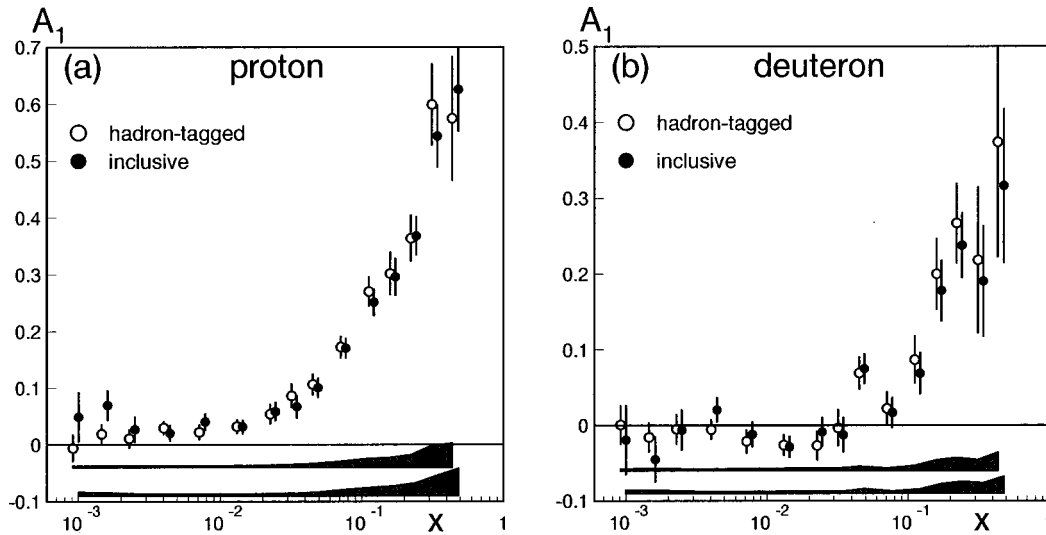


FIG. 5. The values of A_1 for the two types of event selections, inclusive and hadron tagged. The upper shaded bands indicate the systematic uncertainty of A_1 for the hadron-tagged selection, while the lower shaded bands indicate this for the inclusive selection.

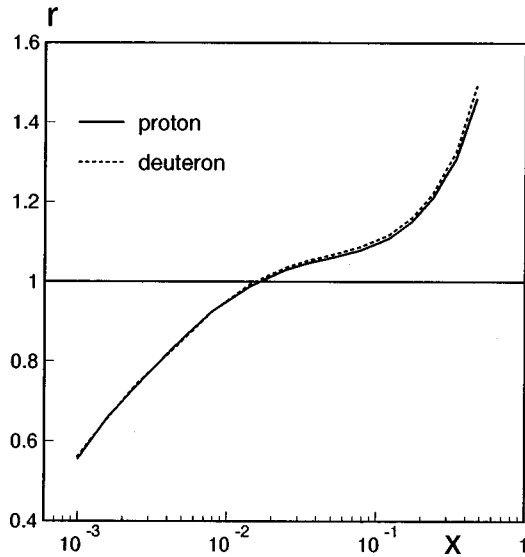


FIG. 6. The ratio r of statistical errors for A_1 from hadron-tagged events and from inclusive events as a function of x , for proton and for deuteron.

B. A_1 for hadron tagged events

The SMC data on polarized protons and polarized deuterons were also analyzed using only hadron-tagged events. The results are presented in Fig. 5 as a function of x .

Most of the systematic errors were treated in the same way as for the inclusive analysis [7]. They arise from the uncertainties of the target and the beam polarizations, the polarized background, the value of R , the neglect of the A_2 contribution, and the momentum resolution. In addition, the uncertainties in the effective dilution factor and the radiative corrections include the uncertainty in $\sigma_{\text{tail}}^{\text{incl}}$, which is taken as 30% of its value. This accounts for events with hard photon radiation, where the available energy for fragmentation into hadrons is reduced, and which may not be tagged. The uncertainty due to acceptance variation with time includes the

effect of changes in the acceptance for both the scattered muon and for the hadrons.

C. Comparison of A_1 for inclusive and hadron-tagged events

The A_1 asymmetries for the two types of event selections, inclusive and hadron tagged, are compared in Fig. 5. The differences are small except for the two lowest x points for the proton data.

As explained before, the results for the event selection with hadron tagging have smaller statistical errors at low x , while the inclusive event selection gives more precise results for high x . This can be seen in Fig. 6, which gives the ratio of the statistical errors for A_1 obtained with the two types of event selections as a function of x .

D. Optimal set of A_1 from SMC data

Figure 6 demonstrates that for $x < 0.02$ the more accurate results for A_1 are obtained by using hadron-tagged events, while for $x > 0.02$ the inclusive events give the more precise result. We therefore take as the optimal set of A_1 values the results from the hadron method for $x < 0.02$ and the results from the inclusive method for $x > 0.02$. This leads to the A_1 values in bins of x presented in Fig. 7 and Tables II and III. The hadron method is used for the lowest 6 x bins for the data shown in Fig. 7. Contributions to the systematic error are detailed in Tables IV and V for each x bin and their quadratic sum is shown as a band in Fig. 7.

The weak Q^2 dependence of A_1^p and A_1^d in each bin of x is presented in Figs. 8 and 9 and Tables VI and VII. From perturbative QCD a different Q^2 behavior is expected for the structure functions F_1 and g_1 , hence $A_1 \approx g_1/F_1$ should be Q^2 dependent. This dependence follows from the Dokshitzer-Gribov-Lipatov-Altarelli-Parisi (DGLAP) equations [26]. It was determined in our QCD analysis, performed in next-to-leading order (NLO), which is presented in the following paper [14]. The results are shown as the solid

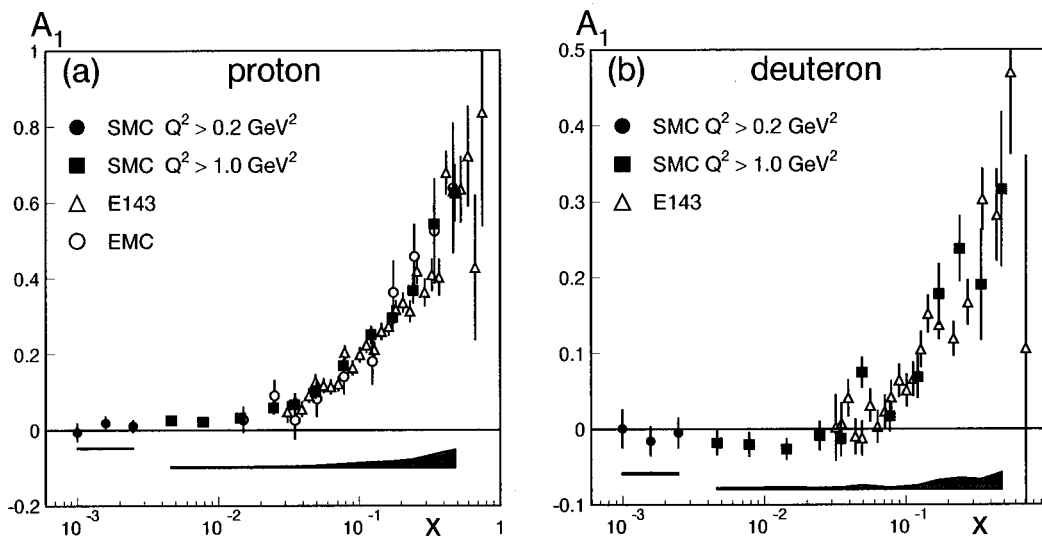


FIG. 7. The optimal set of SMC results for A_1 together with the results from other experiments. Statistical errors are shown as error bars, while the shaded bands below indicate the systematic uncertainty for the SMC measurements.

TABLE II. Optimal set of asymmetries $A_1^p(x)$ from SMC data. The first error is statistical and the second is systematic. The first three bins have $Q^2 > 0.2 \text{ GeV}^2$, while the remaining ones have $Q^2 > 1 \text{ GeV}^2$. Only the $Q^2 > 1 \text{ GeV}^2$ bins are used in the QCD analysis mentioned in Sec. VI.

| x range | $\langle x \rangle$ | $\langle Q^2 \rangle$ (GeV^2) | A_1^p |
|---------------|---------------------|---|------------------------------|
| 0.0008–0.0012 | 0.001 | 0.3 | $-0.004 \pm 0.025 \pm 0.002$ |
| 0.0012–0.002 | 0.002 | 0.5 | $0.021 \pm 0.018 \pm 0.003$ |
| 0.002–0.003 | 0.002 | 0.7 | $0.014 \pm 0.017 \pm 0.003$ |
| 0.003–0.006 | 0.005 | 1.3 | $0.029 \pm 0.014 \pm 0.003$ |
| 0.006–0.010 | 0.008 | 2.1 | $0.026 \pm 0.014 \pm 0.003$ |
| 0.010–0.020 | 0.014 | 3.6 | $0.036 \pm 0.013 \pm 0.003$ |
| 0.020–0.030 | 0.025 | 5.7 | $0.059 \pm 0.017 \pm 0.004$ |
| 0.030–0.040 | 0.035 | 7.8 | $0.068 \pm 0.021 \pm 0.004$ |
| 0.040–0.060 | 0.049 | 10.4 | $0.101 \pm 0.018 \pm 0.006$ |
| 0.060–0.100 | 0.077 | 14.9 | $0.170 \pm 0.018 \pm 0.011$ |
| 0.100–0.150 | 0.122 | 21.3 | $0.252 \pm 0.024 \pm 0.015$ |
| 0.150–0.200 | 0.173 | 27.8 | $0.296 \pm 0.033 \pm 0.018$ |
| 0.200–0.300 | 0.242 | 35.6 | $0.368 \pm 0.034 \pm 0.023$ |
| 0.300–0.400 | 0.342 | 45.9 | $0.544 \pm 0.055 \pm 0.036$ |
| 0.400–0.700 | 0.480 | 58.0 | $0.625 \pm 0.075 \pm 0.048$ |

lines in Figs. 8 and 9 and give a good description of the data. Also the assumption of A_1 having no Q^2 dependence, shown as the dashed lines in these figures, describes the data well.

V. CALCULATION OF g_1

We evaluate g_1 from Eq. (3), using our results for A_1 from Tables II and III, neglecting the contribution from A_2 . The unpolarized structure function F_2 and the ratio R are evaluated at the x and Q^2 values of our measurement of A_1 ,

TABLE IV. Contributions to the systematic error for $A_1^p(x)$ are the uncertainties of the false asymmetry contribution ΔA_{false} due to the time variation of the spectrometer acceptance, the target and the beam polarizations ΔP_t and ΔP_μ , the effective dilution factor $\Delta f'$, the radiative corrections Δrc , the neglect of A_2 , ΔA_2 , the ratio R , ΔR , the momentum resolution ΔMR , and the polarized background from ^{14}N in the ammonia target ΔP_{bg} . The first three bins have $Q^2 > 0.2 \text{ GeV}^2$, while the rest have $Q^2 > 1 \text{ GeV}^2$.

| $\langle x \rangle$ | ΔA_{false} | ΔP_t | ΔP_μ | $\Delta f'$ | Δrc | ΔA_2 | ΔR | ΔMR | ΔP_{bg} |
|---------------------|---------------------------|--------------|----------------|-------------|--------------------|--------------|------------|-------------|------------------------|
| 0.0010 | 0.0019 | 0.0001 | 0.0001 | 0.0002 | 0.0008 | 0.0010 | 0.0002 | 0.0000 | 0.0006 |
| 0.0016 | 0.0019 | 0.0006 | 0.0005 | 0.0012 | 0.0008 | 0.0012 | 0.0007 | 0.0001 | 0.0006 |
| 0.0025 | 0.0019 | 0.0004 | 0.0003 | 0.0008 | 0.0008 | 0.0013 | 0.0004 | 0.0000 | 0.0006 |
| 0.005 | 0.0018 | 0.0009 | 0.0007 | 0.0015 | 0.0009 | 0.0005 | 0.0009 | 0.0000 | 0.0005 |
| 0.008 | 0.0019 | 0.0008 | 0.0006 | 0.0013 | 0.0009 | 0.0007 | 0.0007 | 0.0001 | 0.0005 |
| 0.014 | 0.0020 | 0.0011 | 0.0009 | 0.0017 | 0.0008 | 0.0008 | 0.0013 | 0.0001 | 0.0004 |
| 0.025 | 0.0018 | 0.0018 | 0.0014 | 0.0011 | 0.0007 | 0.0003 | 0.0028 | 0.0002 | 0.0004 |
| 0.035 | 0.0018 | 0.0020 | 0.0016 | 0.0013 | 0.0008 | 0.0003 | 0.0027 | 0.0003 | 0.0004 |
| 0.049 | 0.0019 | 0.0030 | 0.0024 | 0.0019 | 0.0009 | 0.0003 | 0.0041 | 0.0005 | 0.0003 |
| 0.077 | 0.0019 | 0.0051 | 0.0040 | 0.0032 | 0.0009 | 0.0004 | 0.0079 | 0.0008 | 0.0004 |
| 0.122 | 0.0020 | 0.0076 | 0.0059 | 0.0049 | 0.0010 | 0.0005 | 0.0099 | 0.0012 | 0.0008 |
| 0.173 | 0.0021 | 0.0089 | 0.0069 | 0.0059 | 0.0010 | 0.0005 | 0.0118 | 0.0017 | 0.0010 |
| 0.242 | 0.0021 | 0.0110 | 0.0086 | 0.0078 | 0.0010 | 0.0022 | 0.0157 | 0.0023 | 0.0013 |
| 0.342 | 0.0021 | 0.0163 | 0.0127 | 0.0138 | 0.0009 | 0.0025 | 0.0258 | 0.0029 | 0.0017 |
| 0.480 | 0.0021 | 0.0188 | 0.0147 | 0.0223 | 0.0009 | 0.0029 | 0.0348 | 0.0034 | 0.0021 |

TABLE III. Optimal set of asymmetries $A_1^d(x)$ from SMC data, otherwise same explanations as for Table II.

| x range | $\langle x \rangle$ | $\langle Q^2 \rangle$ (GeV^2) | A_1^d |
|---------------|---------------------|---|------------------------------|
| 0.0008–0.0012 | 0.001 | 0.3 | $0.001 \pm 0.026 \pm 0.002$ |
| 0.0012–0.002 | 0.002 | 0.5 | $-0.016 \pm 0.020 \pm 0.003$ |
| 0.002–0.003 | 0.002 | 0.7 | $-0.005 \pm 0.020 \pm 0.002$ |
| 0.003–0.006 | 0.005 | 1.3 | $-0.018 \pm 0.016 \pm 0.002$ |
| 0.006–0.010 | 0.008 | 2.1 | $-0.020 \pm 0.016 \pm 0.003$ |
| 0.010–0.020 | 0.014 | 3.5 | $-0.027 \pm 0.015 \pm 0.003$ |
| 0.020–0.030 | 0.025 | 5.5 | $-0.009 \pm 0.020 \pm 0.003$ |
| 0.030–0.040 | 0.035 | 7.5 | $-0.013 \pm 0.024 \pm 0.003$ |
| 0.040–0.060 | 0.049 | 10.0 | $0.075 \pm 0.021 \pm 0.006$ |
| 0.060–0.100 | 0.077 | 14.4 | $0.017 \pm 0.021 \pm 0.003$ |
| 0.100–0.150 | 0.121 | 20.6 | $0.069 \pm 0.028 \pm 0.006$ |
| 0.150–0.200 | 0.172 | 26.8 | $0.178 \pm 0.041 \pm 0.013$ |
| 0.200–0.300 | 0.241 | 34.3 | $0.238 \pm 0.044 \pm 0.015$ |
| 0.300–0.400 | 0.342 | 43.9 | $0.190 \pm 0.073 \pm 0.014$ |
| 0.400–0.700 | 0.479 | 54.8 | $0.316 \pm 0.102 \pm 0.022$ |

using the parametrizations mentioned in Sec. IV. In Fig. 10 and Tables VIII and IX we present g_1 at the measured Q^2 for the proton and the deuteron. For the first time we show g_1 for data down to $x=0.0008$, which is possible because a valid parametrization of F_2 for this region now exists. In the lowest bin of x we have Q^2 values below 1 GeV^2 .

VI. FIRST MOMENTS OF g_1^p AND g_1^d

We use our data in the kinematic region $Q^2 > 1 \text{ GeV}^2$ (therefore $x > 0.003$) to calculate the first moments of $g_1^{p,d}(x, Q_0^2)$ at a fixed value of $Q^2 = Q_0^2$. The values of

TABLE V. Contributions to the systematic error for $A_1^d(x)$, otherwise same explanations as for Table IV, except that ΔP_{bg} now refers to the contribution from protons in the deuterated butanol target.

| $\langle x \rangle$ | ΔA_{false} | ΔP_t | ΔP_μ | $\Delta f'$ | Δrc | ΔA_2 | ΔR | ΔMR | ΔP_{bg} |
|---------------------|---------------------------|--------------|----------------|-------------|-------------|--------------|------------|-------------|-----------------|
| 0.0010 | 0.0017 | 0.0000 | 0.0000 | 0.0000 | 0.0009 | 0.0009 | 0.0000 | 0.0000 | 0.0002 |
| 0.0016 | 0.0017 | 0.0009 | 0.0004 | 0.0008 | 0.0009 | 0.0010 | 0.0005 | 0.0000 | 0.0002 |
| 0.0025 | 0.0017 | 0.0000 | 0.0002 | 0.0003 | 0.0009 | 0.0013 | 0.0002 | 0.0000 | 0.0002 |
| 0.005 | 0.0016 | 0.0002 | 0.0004 | 0.0008 | 0.0010 | 0.0004 | 0.0006 | 0.0000 | 0.0002 |
| 0.008 | 0.0018 | 0.0011 | 0.0006 | 0.0010 | 0.0010 | 0.0006 | 0.0006 | 0.0000 | 0.0002 |
| 0.014 | 0.0020 | 0.0014 | 0.0006 | 0.0011 | 0.0010 | 0.0007 | 0.0009 | 0.0000 | 0.0002 |
| 0.025 | 0.0019 | 0.0007 | 0.0003 | 0.0002 | 0.0010 | 0.0012 | 0.0004 | 0.0001 | 0.0002 |
| 0.035 | 0.0019 | 0.0003 | 0.0005 | 0.0007 | 0.0010 | 0.0014 | 0.0006 | 0.0001 | 0.0003 |
| 0.049 | 0.0020 | 0.0029 | 0.0020 | 0.0016 | 0.0010 | 0.0016 | 0.0033 | 0.0002 | 0.0004 |
| 0.077 | 0.0021 | 0.0007 | 0.0004 | 0.0000 | 0.0012 | 0.0004 | 0.0008 | 0.0005 | 0.0006 |
| 0.121 | 0.0022 | 0.0031 | 0.0019 | 0.0016 | 0.0012 | 0.0005 | 0.0027 | 0.0008 | 0.0008 |
| 0.172 | 0.0024 | 0.0083 | 0.0045 | 0.0029 | 0.0013 | 0.0006 | 0.0071 | 0.0010 | 0.0011 |
| 0.241 | 0.0025 | 0.0084 | 0.0060 | 0.0038 | 0.0014 | 0.0018 | 0.0101 | 0.0012 | 0.0015 |
| 0.342 | 0.0026 | 0.0069 | 0.0050 | 0.0041 | 0.0012 | 0.0021 | 0.0089 | 0.0013 | 0.0021 |
| 0.479 | 0.0027 | 0.0094 | 0.0074 | 0.0041 | 0.0014 | 0.0024 | 0.0176 | 0.0014 | 0.0027 |

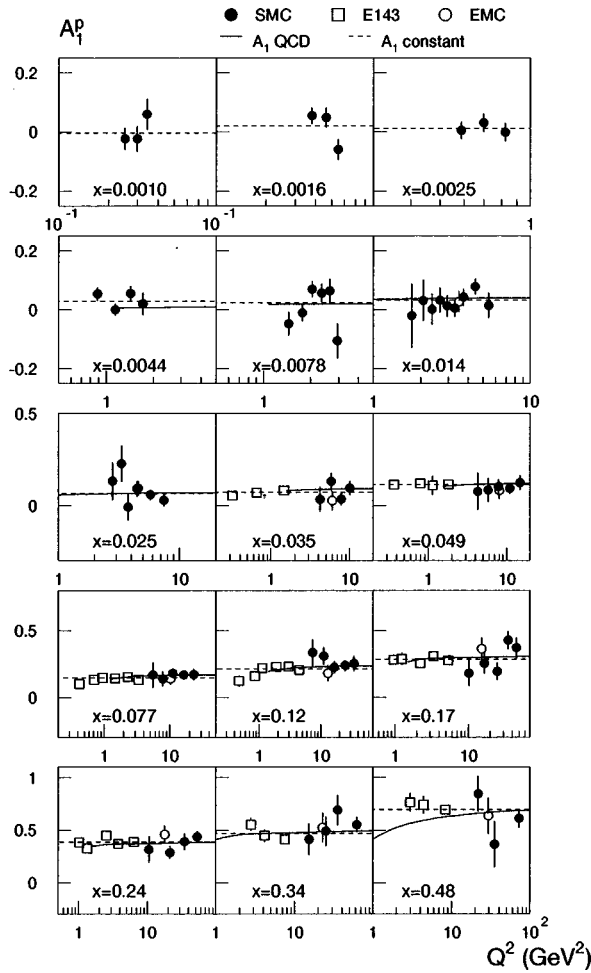
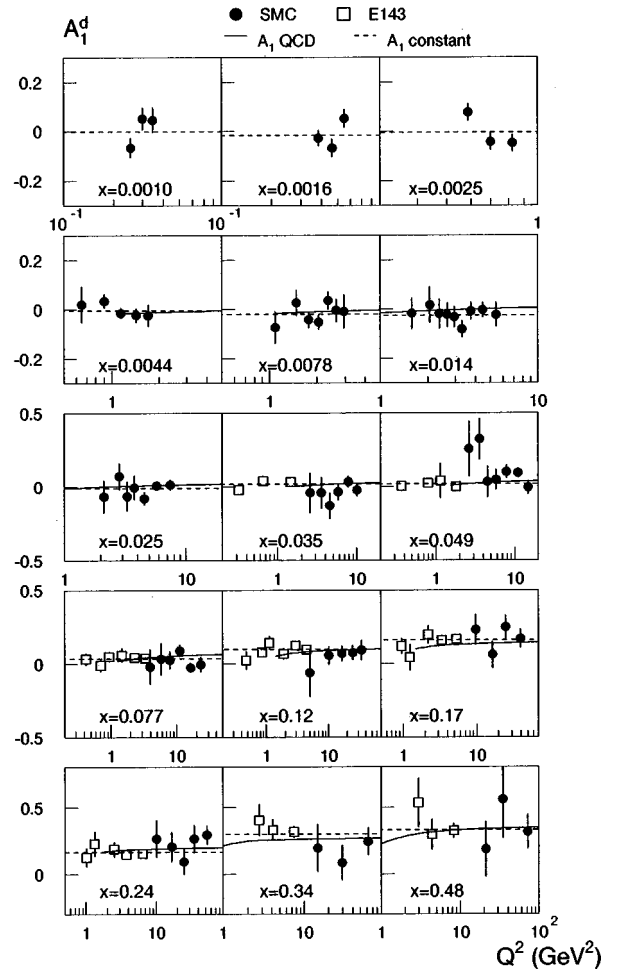

 FIG. 8. A_1^p as a function of Q^2 for different bins of x for the SMC data, where the value of x is the average value in each bin. The EMC and E143 results are also shown for comparison. Error bars show statistical uncertainties. The solid line is a result of the QCD analysis described in our next paper [14] and used in Sec. VI, while the dashed line is the fit assuming no Q^2 dependence.

 FIG. 9. A_1^d as a function of Q^2 for different bins of x for the SMC data, where the value of x is the average value in each bin. The E143 results are also shown for comparison. Other explanations as for Fig. 8.

TABLE VI. Optimal set of asymmetries $A_1^p(x, Q^2)$ from SMC data. The errors are statistical only.

| $\langle x \rangle$ | $\langle Q^2 \rangle$ (GeV ²) | A_1^p | $\langle x \rangle$ | $\langle Q^2 \rangle$ (GeV ²) | A_1^p |
|---------------------|--|--------------------|---------------------|--|-------------------|
| 0.0009 | 0.25 | -0.023 ± 0.037 | 0.0339 | 4.23 | 0.032 ± 0.068 |
| 0.0010 | 0.30 | -0.023 ± 0.043 | 0.0342 | 5.80 | 0.130 ± 0.048 |
| 0.0011 | 0.34 | 0.062 ± 0.051 | 0.0344 | 7.77 | 0.034 ± 0.033 |
| 0.0014 | 0.38 | 0.056 ± 0.028 | 0.0359 | 10.14 | 0.094 ± 0.039 |
| | | | 0.0472 | 4.29 | 0.076 ± 0.101 |
| 0.0016 | 0.46 | 0.051 ± 0.033 | 0.0474 | 5.85 | 0.083 ± 0.064 |
| 0.0018 | 0.55 | -0.057 ± 0.034 | 0.0479 | 7.83 | 0.103 ± 0.038 |
| 0.0022 | 0.59 | 0.006 ± 0.029 | 0.0485 | 10.95 | 0.091 ± 0.027 |
| 0.0025 | 0.70 | 0.032 ± 0.030 | 0.0527 | 14.72 | 0.123 ± 0.040 |
| 0.0028 | 0.82 | -0.002 ± 0.031 | 0.0737 | 5.47 | 0.168 ± 0.094 |
| 0.0035 | 0.89 | 0.055 ± 0.023 | 0.0744 | 7.88 | 0.138 ± 0.056 |
| 0.0042 | 1.14 | 0.003 ± 0.019 | 0.0750 | 11.08 | 0.181 ± 0.036 |
| 0.0050 | 1.44 | 0.059 ± 0.024 | 0.0762 | 16.30 | 0.170 ± 0.028 |
| 0.0056 | 1.71 | 0.025 ± 0.038 | 0.0856 | 23.10 | 0.172 ± 0.043 |
| 0.0069 | 1.44 | -0.047 ± 0.040 | 0.1189 | 7.40 | 0.335 ± 0.098 |
| 0.0071 | 1.76 | -0.007 ± 0.029 | 0.1196 | 11.14 | 0.309 ± 0.065 |
| 0.0075 | 2.04 | 0.073 ± 0.027 | 0.1200 | 16.48 | 0.225 ± 0.045 |
| 0.0083 | 2.34 | 0.060 ± 0.032 | 0.1205 | 24.82 | 0.239 ± 0.041 |
| 0.0090 | 2.64 | 0.069 ± 0.041 | 0.1293 | 34.31 | 0.254 ± 0.057 |
| 0.0095 | 2.94 | -0.098 ± 0.059 | 0.1711 | 10.18 | 0.179 ± 0.096 |
| 0.0114 | 1.75 | -0.021 ± 0.109 | 0.1715 | 16.51 | 0.253 ± 0.076 |
| 0.0119 | 2.07 | 0.032 ± 0.070 | 0.1717 | 24.89 | 0.194 ± 0.065 |
| 0.0123 | 2.36 | 0.003 ± 0.052 | 0.1718 | 34.94 | 0.427 ± 0.069 |
| 0.0125 | 2.66 | 0.032 ± 0.043 | 0.1770 | 45.47 | 0.371 ± 0.077 |
| 0.0126 | 2.96 | 0.015 ± 0.037 | 0.2368 | 10.53 | 0.317 ± 0.125 |
| 0.0131 | 3.30 | 0.009 ± 0.030 | 0.2392 | 21.49 | 0.288 ± 0.059 |
| 0.0145 | 3.74 | 0.046 ± 0.030 | 0.2398 | 34.94 | 0.391 ± 0.080 |
| 0.0163 | 4.43 | 0.084 ± 0.027 | 0.2462 | 52.75 | 0.438 ± 0.054 |
| 0.0183 | 5.44 | 0.022 ± 0.043 | 0.3383 | 15.25 | 0.413 ± 0.150 |
| 0.0231 | 2.78 | 0.132 ± 0.104 | 0.3404 | 25.00 | 0.491 ± 0.142 |
| 0.0236 | 3.31 | 0.227 ± 0.099 | 0.3407 | 34.97 | 0.691 ± 0.145 |
| 0.0235 | 3.77 | -0.008 ± 0.072 | 0.3436 | 61.83 | 0.553 ± 0.074 |
| 0.0237 | 4.54 | 0.093 ± 0.039 | 0.4688 | 21.85 | 0.845 ± 0.170 |
| 0.0241 | 5.75 | 0.058 ± 0.028 | 0.4751 | 34.98 | 0.366 ± 0.218 |
| 0.0263 | 7.41 | 0.028 ± 0.032 | 0.4843 | 72.10 | 0.614 ± 0.090 |

$g_1(x, Q_0^2)$ at the fixed Q_0^2 are determined from $g_1(x, Q^2)$ at the measured x and Q^2 as

$$g_1(x, Q_0^2) = g_1(x, Q^2) + [g_1^{\text{fit}}(x, Q_0^2) - g_1^{\text{fit}}(x, Q^2)], \quad (8)$$

where g_1^{fit} is a result of our NLO QCD analysis. This analysis is presented in Ref. [14]. We choose $Q_0^2 = 10 \text{ GeV}^2$ since it is close to the average Q^2 of our data. The resulting values of $g_1(x, Q_0^2)$ are given in Tables VIII and IX. In the measured range $0.003 < x < 0.7$ the contributions to the first moments of the proton and the deuteron structure functions are calculated neglecting the x dependence of A_1 within a given x bin.

The results at $Q_0^2 = 10 \text{ GeV}^2$ are

$$\int_{0.003}^{0.7} g_1^p(x, Q_0^2) dx = 0.131 \pm 0.005 \pm 0.006 \pm 0.004, \quad (9)$$

$$\int_{0.003}^{0.7} g_1^d(x, Q_0^2) dx = 0.037 \pm 0.006 \pm 0.003 \pm 0.003, \quad (10)$$

where the first uncertainty is statistical, the second is systematic and the third is due to the uncertainty in the Q^2 evolution. The errors of g_1 are correlated between x bins and this correlation was taken into account when calculating systematic and theoretical uncertainties of the integrals. The contributions from different sources of uncertainty, detailed in

TABLE VII. Optimal set of asymmetries $A_1^d(x, Q^2)$ from SMC data. The errors are statistical only.

| $\langle x \rangle$ | $\langle Q^2 \rangle$ (GeV ²) | A_1^d | $\langle x \rangle$ | $\langle Q^2 \rangle$ (GeV ²) | A_1^d |
|---------------------|--|--------------|---------------------|--|--------------|
| 0.0009 | 0.25 | -0.067±0.040 | 0.0342 | 3.57 | -0.042±0.108 |
| 0.0010 | 0.30 | 0.052±0.046 | 0.0342 | 4.54 | -0.129±0.089 |
| 0.0011 | 0.34 | 0.046±0.052 | 0.0342 | 5.80 | -0.036±0.056 |
| 0.0014 | 0.38 | -0.028±0.032 | 0.0344 | 7.78 | 0.033±0.038 |
| 0.0016 | 0.46 | -0.069±0.037 | 0.0359 | 10.13 | -0.023±0.045 |
| 0.0018 | 0.55 | 0.052±0.037 | 0.0476 | 2.63 | 0.257±0.187 |
| 0.0022 | 0.59 | 0.076±0.035 | 0.0476 | 3.59 | 0.322±0.140 |
| 0.0025 | 0.70 | -0.043±0.035 | 0.0479 | 4.52 | 0.034±0.108 |
| 0.0027 | 0.82 | -0.049±0.035 | 0.0477 | 5.83 | 0.047±0.069 |
| 0.0038 | 0.65 | 0.020±0.073 | 0.0480 | 7.82 | 0.101±0.044 |
| 0.0035 | 0.90 | 0.034±0.029 | 0.0484 | 10.95 | 0.093±0.032 |
| 0.0042 | 1.14 | -0.015±0.023 | 0.0527 | 14.72 | -0.006±0.047 |
| 0.0050 | 1.44 | -0.024±0.028 | 0.0744 | 3.95 | -0.019±0.120 |
| 0.0056 | 1.71 | -0.025±0.045 | 0.0743 | 5.82 | 0.034±0.108 |
| 0.0074 | 1.09 | -0.074±0.066 | 0.0746 | 7.85 | 0.026±0.062 |
| 0.0071 | 1.47 | 0.026±0.052 | 0.0753 | 11.05 | 0.090±0.041 |
| 0.0071 | 1.77 | -0.043±0.034 | 0.0760 | 16.30 | -0.025±0.033 |
| 0.0075 | 2.04 | -0.053±0.031 | 0.0855 | 23.07 | -0.004±0.051 |
| 0.0083 | 2.34 | 0.035±0.037 | 0.1187 | 5.00 | -0.062±0.162 |
| 0.0090 | 2.64 | -0.005±0.047 | 0.1194 | 10.23 | 0.056±0.063 |
| 0.0095 | 2.94 | -0.010±0.069 | 0.1201 | 16.43 | 0.069±0.054 |
| 0.0128 | 1.59 | -0.018±0.064 | 0.1203 | 24.82 | 0.076±0.050 |
| 0.0131 | 2.06 | 0.016±0.074 | 0.1289 | 34.25 | 0.093±0.069 |
| 0.0128 | 2.36 | -0.019±0.061 | 0.1709 | 9.72 | 0.231±0.106 |
| 0.0125 | 2.66 | -0.024±0.050 | 0.1714 | 16.47 | 0.062±0.091 |
| 0.0125 | 2.96 | -0.033±0.043 | 0.1716 | 24.84 | 0.249±0.081 |
| 0.0130 | 3.30 | -0.082±0.035 | 0.1739 | 39.62 | 0.171±0.065 |
| 0.0144 | 3.74 | -0.008±0.035 | 0.2368 | 10.06 | 0.264±0.140 |
| 0.0163 | 4.44 | -0.003±0.031 | 0.2386 | 16.52 | 0.205±0.111 |
| 0.0184 | 5.44 | -0.023±0.050 | 0.2393 | 24.86 | 0.093±0.096 |
| 0.0237 | 2.13 | -0.067±0.110 | 0.2391 | 34.93 | 0.265±0.105 |
| 0.0239 | 2.82 | 0.071±0.091 | 0.2454 | 52.73 | 0.294±0.072 |
| 0.0242 | 3.30 | -0.063±0.102 | 0.3388 | 14.77 | 0.194±0.178 |
| 0.0239 | 3.76 | -0.004±0.084 | 0.3404 | 29.55 | 0.084±0.132 |
| 0.0237 | 4.54 | -0.079±0.045 | 0.3431 | 61.80 | 0.244±0.102 |
| 0.0241 | 5.75 | 0.008±0.032 | 0.4706 | 21.18 | 0.185±0.208 |
| 0.0263 | 7.41 | 0.013±0.037 | 0.4763 | 34.87 | 0.558±0.289 |
| 0.0341 | 2.59 | -0.042±0.138 | 0.4827 | 71.76 | 0.317±0.129 |

Table X, were added in quadrature when computing the total errors. In addition to the uncertainties for A_1 given in Tables IV and V, for the calculation of the first moments we consider also contributions from the kinematic resolution and the error due to the approximations in the asymmetry evaluation procedure. The latter was estimated with a Monte Carlo simulation of this procedure. In our previous publications the central values for the integrals in Eqs. (9) and (10) were 0.130 [7] and 0.041 [11], respectively. The difference is mainly due to the updated beam polarization.

The first moments of g_1 are

$$\int_0^1 g_1^p(x, Q_0^2) dx = 0.120 \pm 0.005 \pm 0.006 \pm 0.014, \quad (11)$$

$$\int_0^1 g_1^d(x, Q_0^2) dx = 0.019 \pm 0.006 \pm 0.003 \pm 0.013. \quad (12)$$

They are obtained by combining the results from Eqs. (9) and (10) with the contributions from the unmeasured ranges, which were calculated from the parametrizations of parton

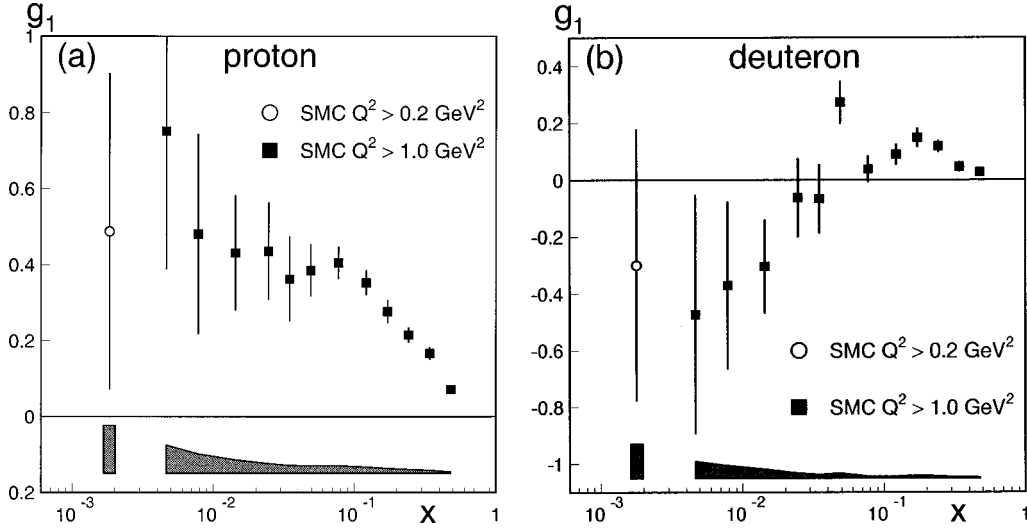


FIG. 10. The optimal set of SMC results of g_1 : (a) for proton and (b) for deuteron. Statistical errors are shown as error bars while the shaded band below indicates the systematic uncertainty. The $Q^2 > 0.2 \text{ GeV}^2$ result was obtained by combining the lowest three A_1 bins.

distributions from our NLO QCD analysis [14]. In the calculation of the total error we have taken into account that the value in the measured region affects the contributions from the unmeasured regions.

VII. THE NONSINGLET STRUCTURE FUNCTION g_1^{NS}

The flavor nonsinglet combination of the spin-dependent structure functions $g_1^{\text{NS}} = g_1^p - g_1^n$ is an interesting quantity because a rigorous QCD prediction exists for its first moment. This sum rule was derived, in the limit of infinite momentum transfer, by Bjorken [1] using current algebra and isospin symmetry.

A. Comparison of $g_1^p - g_1^n$ and $F_1^p - F_1^n$

In our experiment $g_1^p(x, Q^2)$ and $g_1^d(x, Q^2)$ are measured in the same bins of x and Q^2 . We evaluate $g_1^{\text{NS}}(x, Q^2)$ from

$$g_1^{\text{NS}}(x, Q^2) = 2 \left[g_1^p(x, Q^2) - \frac{g_1^d(x, Q^2)}{[1 - (3/2)\omega_D]} \right], \quad (13)$$

where ω_D is the probability of the deuteron to be in the D state. As in our previous publications we have used $\omega_D = 0.05 \pm 0.01$, which covers most of the published values [27].

The results are given in Table XI with statistical and systematic errors. In calculating the systematic error the contributions from the beam polarization, the dilution factor, and R were treated as correlated between proton and deuteron, whereas the other contributions to the systematic error were treated as uncorrelated [28].

The results for g_1^{NS} are shown in Fig. 11, together with g_1^{NS} from the E143 experiment calculated from their values of g_1^p and g_1^d [29]. For both data sets the points are shown at the measured Q^2 . In the same figure we show the nonsinglet

TABLE VIII. The spin-dependent structure function g_1^p at the measured Q^2 and for $Q^2 > 1 \text{ GeV}^2$, where the QCD evolution is applicable, g_1^p evolved to $Q_0^2 = 10 \text{ GeV}^2$. The first bin, which has $Q^2 > 0.2 \text{ GeV}^2$, was obtained by combining the lowest three A_1 bins from Table II. The first error is statistical and the second is systematic. In the last column the third error indicates the uncertainty in the QCD evolution.

| x range | $\langle x \rangle$ | $\langle Q^2 \rangle$ (GeV^2) | g_1^p | $g_1^p(Q_0^2 = 10 \text{ GeV}^2)$ |
|--------------|---------------------|---|--------------------------|-----------------------------------|
| 0.0008–0.003 | 0.002 | 0.5 | $0.49 \pm 0.42 \pm 0.13$ | |
| 0.003–0.006 | 0.005 | 1.3 | $0.75 \pm 0.36 \pm 0.07$ | $1.19 \pm 0.36 \pm 0.07 \pm 0.56$ |
| 0.006–0.010 | 0.008 | 2.1 | $0.48 \pm 0.26 \pm 0.05$ | $0.72 \pm 0.26 \pm 0.05 \pm 0.25$ |
| 0.010–0.020 | 0.014 | 3.6 | $0.43 \pm 0.15 \pm 0.03$ | $0.59 \pm 0.15 \pm 0.03 \pm 0.07$ |
| 0.020–0.030 | 0.025 | 5.7 | $0.43 \pm 0.13 \pm 0.03$ | $0.50 \pm 0.13 \pm 0.03 \pm 0.02$ |
| 0.030–0.040 | 0.035 | 7.8 | $0.36 \pm 0.11 \pm 0.02$ | $0.39 \pm 0.11 \pm 0.02 \pm 0.01$ |
| 0.040–0.060 | 0.049 | 10.4 | $0.38 \pm 0.07 \pm 0.02$ | $0.38 \pm 0.07 \pm 0.02 \pm 0.00$ |
| 0.060–0.100 | 0.077 | 14.9 | $0.41 \pm 0.04 \pm 0.02$ | $0.39 \pm 0.04 \pm 0.02 \pm 0.00$ |
| 0.100–0.150 | 0.122 | 21.3 | $0.35 \pm 0.03 \pm 0.02$ | $0.33 \pm 0.03 \pm 0.02 \pm 0.00$ |
| 0.150–0.200 | 0.173 | 27.8 | $0.28 \pm 0.03 \pm 0.01$ | $0.27 \pm 0.03 \pm 0.01 \pm 0.00$ |
| 0.200–0.300 | 0.242 | 35.6 | $0.21 \pm 0.02 \pm 0.01$ | $0.22 \pm 0.02 \pm 0.01 \pm 0.01$ |
| 0.300–0.400 | 0.342 | 45.9 | $0.17 \pm 0.02 \pm 0.01$ | $0.18 \pm 0.02 \pm 0.01 \pm 0.00$ |
| 0.400–0.700 | 0.480 | 58.0 | $0.07 \pm 0.01 \pm 0.00$ | $0.09 \pm 0.01 \pm 0.00 \pm 0.00$ |

TABLE IX. The spin-dependent structure function g_1^d at the measured Q^2 and for $Q^2 > 1 \text{ GeV}^2$, where the QCD evolution is applicable, g_1^d evolved to $Q_0^2 = 10 \text{ GeV}^2$. Other explanations as for Table VIII.

| x range | $\langle x \rangle$ | $\langle Q^2 \rangle$ (GeV^2) | g_1^d | $g_1^d(Q_0^2 = 10 \text{ GeV}^2)$ |
|--------------|---------------------|---|---------------------------|------------------------------------|
| 0.0008–0.003 | 0.002 | 0.5 | $-0.30 \pm 0.48 \pm 0.12$ | |
| 0.003–0.006 | 0.005 | 1.3 | $-0.47 \pm 0.42 \pm 0.06$ | $-0.30 \pm 0.42 \pm 0.06 \pm 0.49$ |
| 0.006–0.010 | 0.008 | 2.1 | $-0.37 \pm 0.30 \pm 0.04$ | $-0.22 \pm 0.30 \pm 0.04 \pm 0.22$ |
| 0.010–0.020 | 0.014 | 3.5 | $-0.30 \pm 0.17 \pm 0.03$ | $-0.22 \pm 0.17 \pm 0.03 \pm 0.06$ |
| 0.020–0.030 | 0.025 | 5.5 | $-0.06 \pm 0.14 \pm 0.02$ | $-0.02 \pm 0.14 \pm 0.02 \pm 0.02$ |
| 0.030–0.040 | 0.035 | 7.5 | $-0.07 \pm 0.12 \pm 0.01$ | $-0.05 \pm 0.12 \pm 0.01 \pm 0.01$ |
| 0.040–0.060 | 0.049 | 10.0 | $0.27 \pm 0.08 \pm 0.02$ | $0.27 \pm 0.08 \pm 0.02 \pm 0.00$ |
| 0.060–0.100 | 0.077 | 14.4 | $0.04 \pm 0.05 \pm 0.01$ | $0.03 \pm 0.05 \pm 0.01 \pm 0.00$ |
| 0.100–0.150 | 0.121 | 20.6 | $0.09 \pm 0.04 \pm 0.01$ | $0.08 \pm 0.04 \pm 0.01 \pm 0.00$ |
| 0.150–0.200 | 0.172 | 26.8 | $0.15 \pm 0.03 \pm 0.01$ | $0.14 \pm 0.03 \pm 0.01 \pm 0.00$ |
| 0.200–0.300 | 0.241 | 34.3 | $0.12 \pm 0.02 \pm 0.01$ | $0.12 \pm 0.02 \pm 0.01 \pm 0.00$ |
| 0.300–0.400 | 0.342 | 43.9 | $0.05 \pm 0.02 \pm 0.00$ | $0.05 \pm 0.02 \pm 0.00 \pm 0.00$ |
| 0.400–0.700 | 0.479 | 54.8 | $0.03 \pm 0.01 \pm 0.00$ | $0.04 \pm 0.01 \pm 0.00 \pm 0.00$ |

spin-independent structure function $F_1^{\text{NS}} = F_1^p - F_1^n$ calculated from the measurements of the ratio F_2^d/F_2^p [30], a fit to the data for F_2^p , described in the Appendix, and the values of the function R [24,25]. The Q^2 range of the F_1^{NS} points corresponds approximately to the range covered by the SMC data. The nonsinglet g_1^{NS} (F_1^{NS}) is proportional to the difference of the polarized (unpolarized) u -valence quark and d -valence quark distributions. There may also be a flavor symmetry violating contribution from the nucleon sea, as has been observed in the unpolarized case [31–34]. A possibility that the mechanism of flavor symmetry violations in polarized data may be related to that of the observed violations in the unpolarized case has been discussed in Ref. [35]. It is interesting that the shapes of the nonsinglet part of the polarized and unpolarized structure functions are very similar. The consequences of this similarity for parton distributions in LO and

TABLE X. The sources of uncertainties for the integrals of g_1^p and g_1^d in the measured region $0.003 < x < 0.7$.

| Source of the error | $\Delta\Gamma_1^p$ | $\Delta\Gamma_1^d$ |
|------------------------|--------------------|--------------------|
| Target polarization | 0.0037 | 0.0012 |
| Beam polarization | 0.0029 | 0.0008 |
| Dilution factor | 0.0027 | 0.0006 |
| Uncertainty in F_2 | 0.0023 | 0.0010 |
| Acceptance variation | 0.0015 | 0.0014 |
| Radiative corrections | 0.0007 | 0.0008 |
| Asymmetry evaluation | 0.0006 | 0.0006 |
| Neglect of A_2 | 0.0005 | 0.0006 |
| Polarized background | 0.0005 | 0.0004 |
| Kinematic resolution | 0.0003 | 0.0003 |
| Momentum measurement | 0.0003 | 0.0001 |
| Uncertainty on R | 0.0000 | 0.0000 |
| Total systematic error | 0.0062 | 0.0026 |
| Evolution | 0.0036 | 0.0027 |
| Statistics | 0.0052 | 0.0057 |

NLO have been discussed in Ref. [36]. It should be noted that the polarized nonsinglet distribution is not bounded by the unpolarized nonsinglet but by $F_1^p + F_1^n$. We observe that g_1^{NS} is larger than F_1^{NS} .

B. Q^2 evolution of g_1^{NS}

The flavor nonsinglet combination g_1^{NS} decouples from the singlet and the gluon sectors, and therefore evolves in a different way than g_1^p and g_1^n separately. To calculate its Q^2 evolution only the parametrization of $g_1^{\text{NS}}(x)$ is needed. The evolution to a common Q_0^2 was done by three different methods. The first used the Q^2 dependence of the more accurately measured F_1^{NS} . The Q^2 evolution of g_1^{NS} and F_1^{NS} is expected to be the same since the x distributions are similar and the unpolarized and polarized nonsinglet splitting functions are identical.² The second method evolved the data using the nonsinglet part from the NLO QCD fit [14] already used in Sec. VI to evolve $g_1^{p,d}$ to the common Q_0^2 . The third method used a simpler QCD fit, restricted to the nonsinglet sector [14].

Figure 12 shows $g_1^{\text{NS}}(x, Q^2)$ in each x bin at its average value of Q^2 and evolved to $Q_0^2 = 10 \text{ GeV}^2$ using the nonsinglet fit (method 3) mentioned above. The changes of g_1^{NS} due to the Q^2 evolution are small (compared to the statistical errors). The values of $g_1^{\text{NS}}(x, Q_0^2)$ obtained with the third method are given in Table XI. The evolution calculated with methods 1 and 2 gave values very close to those obtained with method 3. The systematic errors due to Q^2 evolution given in Table XI cover the results from the three methods.

C. First moment of g_1^{NS}

The first moment of g_1^{NS} is calculated in three parts: from our data in the measured region $0.003 < x < 0.7$ and those

²The splitting functions are identical because for massless quarks helicity is conserved at the quark-gluon vertex and gluon bremsstrahlung is the only relevant process here.

TABLE XI. The nonsinglet structure function g_1^{NS} and their uncertainties (shown only with 2 significant digits after the decimal points) calculated from the measured g_1^p and g_1^d at the measured Q^2 and evolved to $Q_0^2=10 \text{ GeV}^2$. The first error is statistical and the second is systematic. In the last column the third error indicates the uncertainty in the QCD evolution.

| x range | $\langle x \rangle$ | $\langle Q^2 \rangle$ (GeV^2) | g_1^{NS} | $g_1^{\text{NS}} (Q_0^2=10 \text{ GeV}^2)$ |
|-------------|---------------------|---|--------------------------|--|
| 0.003–0.006 | 0.005 | 1.3 | $2.53 \pm 1.17 \pm 0.21$ | $3.04 \pm 1.17 \pm 0.21 \pm 0.01$ |
| 0.006–0.010 | 0.008 | 2.1 | $1.76 \pm 0.83 \pm 0.16$ | $2.06 \pm 0.83 \pm 0.16 \pm 0.04$ |
| 0.010–0.020 | 0.014 | 3.6 | $1.52 \pm 0.47 \pm 0.12$ | $1.66 \pm 0.47 \pm 0.12 \pm 0.02$ |
| 0.020–0.030 | 0.025 | 5.6 | $1.00 \pm 0.40 \pm 0.07$ | $1.05 \pm 0.40 \pm 0.07 \pm 0.01$ |
| 0.030–0.040 | 0.035 | 7.6 | $0.87 \pm 0.35 \pm 0.06$ | $0.88 \pm 0.35 \pm 0.06 \pm 0.00$ |
| 0.040–0.060 | 0.049 | 10.2 | $0.18 \pm 0.21 \pm 0.05$ | $0.18 \pm 0.21 \pm 0.05 \pm 0.00$ |
| 0.060–0.100 | 0.077 | 14.6 | $0.73 \pm 0.13 \pm 0.04$ | $0.72 \pm 0.13 \pm 0.04 \pm 0.00$ |
| 0.100–0.150 | 0.122 | 21.0 | $0.51 \pm 0.10 \pm 0.03$ | $0.50 \pm 0.10 \pm 0.03 \pm 0.00$ |
| 0.150–0.200 | 0.173 | 27.3 | $0.23 \pm 0.10 \pm 0.03$ | $0.23 \pm 0.10 \pm 0.03 \pm 0.00$ |
| 0.200–0.300 | 0.242 | 34.9 | $0.17 \pm 0.06 \pm 0.02$ | $0.18 \pm 0.06 \pm 0.02 \pm 0.00$ |
| 0.300–0.400 | 0.342 | 44.9 | $0.23 \pm 0.05 \pm 0.02$ | $0.24 \pm 0.05 \pm 0.02 \pm 0.01$ |
| 0.400–0.700 | 0.480 | 56.4 | $0.09 \pm 0.03 \pm 0.01$ | $0.10 \pm 0.03 \pm 0.01 \pm 0.00$ |

from the unmeasured regions towards the boundaries $x=0$ and $x=1$. In the measured region, the contribution from each x -bin is calculated assuming that the x dependence of g_1^{NS} and F_1^{NS} is the same within the bin. The contributions are summed giving the integral in the measured range at $Q_0^2=10 \text{ GeV}^2$

$$\int_{0.003}^{0.7} g_1^{\text{NS}} dx = 0.184 \pm 0.016 \pm 0.014 \pm 0.001, \quad (14)$$

where the first error is statistical, the second is systematic, and the third is an evolution error based on errors given in Table XI. The total error on the integral in the measured range is 12% of its value. The contributions from the unmeasured regions are calculated from the parametrization of g_1^{NS} obtained in the QCD analysis in Ref. [14]. They are: 0.010 ± 0.003 for $x < 0.003$ and 0.004 ± 0.001 for $x > 0.7$.

The first moment of g_1^{NS} thus amounts to

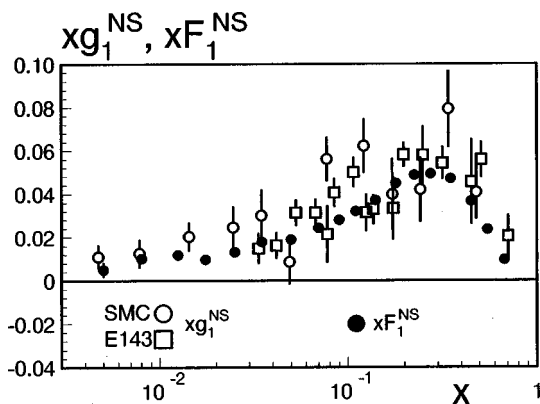


FIG. 11. The nonsinglet functions xg_1^{NS} and xF_1^{NS} . Both functions are presented at the measured Q^2 of the experiments. The errors are statistical only.

$$\int_0^1 g_1^{\text{NS}} dx = 0.198 \pm 0.023 \quad (Q_0^2=10 \text{ GeV}^2). \quad (15)$$

The value of the nonsinglet first moment given in Eq. (15) is in good agreement with the theoretical prediction of 0.186 ± 0.003 at $Q_0^2=10 \text{ GeV}^2$. A more general discussion of the test of the Bjorken sum rule including different evaluations in the framework of perturbative QCD is presented in Ref. [14].

VIII. SUMMARY

This paper concludes the SMC analysis of the virtual photon-proton and virtual photon-deuteron spin asymmetries $A_1^p(x, Q^2)$ and $A_1^d(x, Q^2)$ measured in the deep inelastic scattering of polarized muons on polarized protons and polarized deuterons at incident muon energies of 100 and 190 GeV.

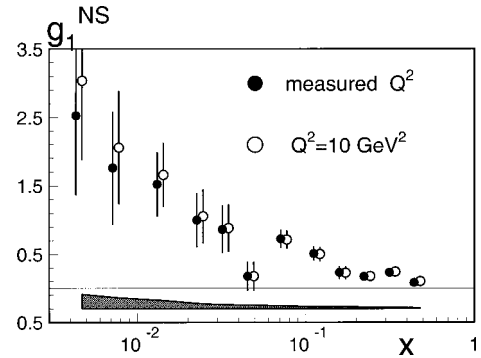


FIG. 12. The nonsinglet function g_1^{NS} as a function of x given at the measured Q^2 and evolved to $Q_0^2=10 \text{ GeV}^2$ with the method described in the text as the third method. Statistical errors are shown as error bars while the shaded band below indicates systematic uncertainty.

The final analysis included a reanalysis of the inclusive data and incorporated an asymmetry determination based on the hadron method, where the presence of at least one hadron in the final state of the muon-nucleon interaction was required. Such a selection removes a part of the background at low x and hence improves the statistical accuracy there. The hadron method was thus used for $x < 0.02$ while the inclusive method was used for $x > 0.02$ in the determination of the final set of results for the asymmetries and the spin-dependent structure functions $g_1^p(x, Q^2)$ and $g_1^d(x, Q^2)$.

These final results, which cover the kinematic range $0.0008 < x < 0.7$ and $0.2 < Q^2 < 100 \text{ GeV}^2$, have been presented. They are consistent with the previously published SMC results [2,6,7,9–11] and supersede them. The final results have been tabulated in bins of x and Q^2 , and the individual contributions to the systematic error for A_1 have been given in bins of x . The analysis of events collected with a special trigger, which requires a signal from the hadron calorimeter in addition to the detection of a scattered muon, and allows measurements down to $x = 0.0001$, mainly for $Q^2 < 1 \text{ GeV}^2$, is in progress.

The spin-dependent flavor nonsinglet structure function g_1^{NS} at the measured Q^2 was compared to the spin-independent nonsinglet structure function F_1^{NS} . Integrals of $g_1^{p,d}(x, Q_0^2 = 10 \text{ GeV}^2)$ and $g_1^{\text{NS}}(x, Q_0^2 = 10 \text{ GeV}^2)$ over the measured range were calculated using SMC data with $Q^2 > 1 \text{ GeV}^2$. The first moments of g_1^p , g_1^d , and g_1^{NS} , including contributions from the unmeasured ranges obtained from the QCD analysis [14], have been given.

ACKNOWLEDGMENTS

We wish to thank our host laboratory CERN for providing major and efficient support for our experiment and an exciting and pleasant environment in which to do it. In particular, we thank J. V. Allaby, P. Darriulat, F. Dydak, L. Foa, G. Goggi, H. J. Hilke, and H. Wenninger for substantial support and constant advice. We also wish to thank L. Gatignon and the SPS Division for providing us with an excellent beam, the LHC-ECR group for efficient cryogenics support, and J. M. Demolis for all his technical support. We also thank all those people in our home institutions who have contributed to the construction and maintenance of our equipment, especially A. Daël, J. C. Languillat, and C. Curé from DAPNIA/Saclay for providing us with the high performance target superconducting magnet, Y. Lefèvre and J. Homma from NIKHEF for their contributions to the construction of the dilution refrigerator, and E. Kok for his contributions to the electronics and the data taking. It is a pleasure to thank G. Altarelli, R. D. Ball, F. E. Close, J. Ellis, D. de Florian, S. Forte, T. Gehrmann, B. L. Ioffe, R. L. Jaffe, M. Karliner, J. Kuti, E. Leader, A. H. Mueller, G. Ridolfi, and W. Vogel-sang for numerous valuable discussions and encouragement over many years. This work was supported by Bundesministerium für Bildung, Wissenschaft, Forschung und Technologie, partially supported by TUBITAK and the Center for Turkish-Balkan Physics Research and Application (Bogziçi University), supported by the U.S. Department of Energy, the U.S. National Science Foundation, Monbusho Grant-in-

Aid for Science Research (International Scientific Research Program and Specially Promoted Research), the National Science Foundation (NWO) of the Netherlands, the Commissariat à l’Energie Atomique, Comision Interministerial de Ciencia y Tecnologia and Xunta de Galicia, the Israel Science Foundation, and Polish State Committee for Scientific Research (KBN) Grant No. 2/P03B/081/14.

APPENDIX

A phenomenological fit for the unpolarized structure functions $F_2^p(x, Q^2)$ and $F_2^d(x, Q^2)$ was performed. Results for proton structure functions from BCDMS [37], E665 [38], NMC [24], SLAC [39], H1 [40], and ZEUS [41] were used to perform a fit for F_2^p . For the fit of F_2^d the results for deuteron structure functions from BCDMS [37], E665 [38], NMC [24], and SLAC [39] and precise measurements of the ratio F_2^d/F_2^p by the NMC [30] were used.

The F_2 parametrization, originally proposed by the BCDMS Collaboration and also used by NMC, is as follows:

$$F_2^{\text{fit}}(x, Q^2) = A(x) \left[\frac{\ln(Q^2/\Lambda^2)}{\ln(Q_0^2/\Lambda^2)} \right]^{B(x)} \left[1 + \frac{C(x)}{Q^2} \right], \quad (\text{A1})$$

where

$$A(x) = x^{a_1}(1-x)^{a_2} [a_3 + a_4(1-x) + a_5(1-x)^2 + a_6(1-x)^3 + a_7(1-x)^4],$$

$$B(x) = b_1 + b_2x + b_3/(x + b_4),$$

$$C(x) = c_1x + c_2x^2 + c_3x^3 + c_4x^4.$$

With $Q_0^2 = 20 \text{ GeV}^2$ and $\Lambda = 0.25 \text{ GeV}$, this 15 parameter function was fitted to F_2^p and F_2^d data separately.

TABLE XII. The values of the parameters of Eq. (A1) for F_2^p and for the upper and lower limits of F_2^p .

| Parameter | F_2^p limits | | |
|-----------|----------------|-------------|-------------|
| | F_2^p | Upper limit | Lower limit |
| a_1 | -0.24997 | -0.24810 | -0.25196 |
| a_2 | 2.3963 | 2.3632 | 2.4297 |
| a_3 | 0.22896 | 0.23643 | 0.21913 |
| a_4 | 0.08498 | -0.03241 | 0.21630 |
| a_5 | 3.8608 | 4.2268 | 3.4645 |
| a_6 | -7.4143 | -7.8120 | -6.9887 |
| a_7 | 3.4342 | 3.5822 | 3.2771 |
| b_1 | 0.11411 | 0.09734 | 0.13074 |
| b_2 | -2.2356 | -2.2254 | -2.2465 |
| b_3 | 0.03115 | 0.03239 | 0.02995 |
| b_4 | 0.02135 | 0.02233 | 0.02039 |
| c_1 | -1.4517 | -1.4361 | -1.4715 |
| c_2 | 8.4745 | 8.1084 | 8.9108 |
| c_3 | -34.379 | -33.306 | -35.714 |
| c_4 | 45.888 | 44.717 | 47.338 |

TABLE XIII. The values of the parameters of Eq. (A1) for F_2^d and for the upper and lower limits of F_2^d .

| Parameter | F_2^d limits | | |
|-----------|----------------|-------------|-------------|
| | F_2^d | Upper limit | Lower limit |
| a_1 | -0.28151 | -0.28047 | -0.28178 |
| a_2 | 1.0115 | 0.82170 | 1.1694 |
| a_3 | 0.08415 | 0.06904 | 0.09973 |
| a_4 | -0.72973 | -0.60191 | -0.85884 |
| a_5 | 2.8647 | 2.2618 | 3.4541 |
| a_6 | -2.5328 | -1.6507 | -3.3995 |
| a_7 | 0.47477 | 0.08909 | 0.86034 |
| b_1 | 0.20040 | 0.18711 | 0.20865 |
| b_2 | -2.5154 | -2.4711 | -2.5475 |
| b_3 | 0.02599 | 0.02802 | 0.02429 |
| b_4 | 0.01858 | 0.01973 | 0.01760 |
| c_1 | -1.3569 | -1.3762 | -1.3513 |
| c_2 | 7.8938 | 7.6113 | 8.3602 |
| c_3 | -29.117 | -27.267 | -37.710 |
| c_4 | 37.657 | 35.100 | 41.106 |

In the fit, the data points were weighted according to their statistical and uncorrelated systematic errors. Additional parameters were included in the fit to describe correlated shifts within the systematic uncertainties and to describe relative normalization shifts between data sets within the normaliza-

tion uncertainties quoted by the experiments. All parameters and the complete covariance matrices were determined in the fits for F_2^p and F_2^d . We used the parameters and the covariance matrices restricted to the 15 parameters of Eq. (A1) to determine the one standard deviation upper and lower limits of F_2 . Both upper and lower limit values for F_2^p and F_2^d were parametrized with the same function.

The fitted parameters for the central values and for the upper and lower limits corresponding to the total uncertainties of F_2 are given in Tables XII and XIII. The fitted parametrizations are only valid in the kinematic range of the data sets, which cover correlated regions in the range of $3.5 \times 10^{-5} < x < 0.85$ and $0.2 < Q^2 < 5000 \text{ GeV}^2$ for F_2^p , and of $0.0009 < x < 0.85$ and $0.2 < Q^2 < 220 \text{ GeV}^2$ for F_2^d . The uncertainty in F_2^d at low x and Q^2 is underestimated due to the fact that the uncertainty of the fitted F_2^p is not taken into account, where the ratio data F_2^d/F_2^p are used. This has a negligible effect on the parameter set which describes the central values of the fitted F_2^d , but the total error given by the upper and lower limits is too small for $Q^2 < 1 \text{ GeV}^2$. For the calculation of the uncertainty of g_1^d due to F_2^d the effect is found to be negligible. Details of the fitting procedure can be found in Ref. [42].

The above parametrizations of F_2 must be used with the proper values of R to reproduce the measured cross sections. We used a parametrization of the values of R measured by the NMC [24] for $x < 0.12$, and for $x > 0.12$ we used the SLAC parametrization given in Ref. [25].

-
- [1] J. D. Bjorken, Phys. Rev. **148**, 1467 (1966); Phys. Rev. D **1**, 1376 (1970).
- [2] SMC Collaboration, D. Adams *et al.*, Phys. Lett. B **329**, 399 (1994); **339**, 332(E) (1994).
- [3] SMC Collaboration, D. Adams *et al.*, Phys. Lett. B **320**, 400 (1994).
- [4] SMC Collaboration, D. Adams *et al.*, Phys. Lett. B **336**, 125 (1994).
- [5] SMC Collaboration, B. Adeva *et al.*, Phys. Lett. B **369**, 93 (1996).
- [6] SMC Collaboration, D. Adams *et al.*, Phys. Rev. D **56**, 5330 (1997).
- [7] SMC Collaboration, B. Adeva *et al.*, Phys. Lett. B **412**, 414 (1997).
- [8] SMC Collaboration, B. Adeva *et al.*, Phys. Lett. B **420**, 180 (1998).
- [9] SMC Collaboration, B. Adeva *et al.*, Phys. Lett. B **302**, 533 (1993).
- [10] SMC Collaboration, D. Adams *et al.*, Phys. Lett. B **357**, 248 (1995).
- [11] SMC Collaboration, D. Adams *et al.*, Phys. Lett. B **396**, 338 (1997).
- [12] NMC Collaboration, M. Arneodo *et al.*, Nucl. Phys. **B441**, 12 (1995).
- [13] E665 Collaboration, M. R. Adams *et al.*, Phys. Lett. B **309**, 477 (1993); **287**, 375 (1992).
- [14] SMC Collaboration, B. Adeva *et al.*, following paper, Phys. Rev. D **58**, 112002 (1998).
- [15] SMC Collaboration, B. Adeva *et al.*, ‘‘Measurement of the SMC Muon Beam Polarization Using the Asymmetry in the Elastic Scattering off Polarized Electrons’’ (in preparation).
- [16] B. Adeva *et al.*, Nucl. Instrum. Methods Phys. Res. A **343**, 363 (1994).
- [17] SMC Collaboration, B. Adeva *et al.*, ‘‘Measurement of the SMC Muon Beam Polarization from Decay Energy Spectrum of the Decay Positrons’’ (in preparation); J. Cranshaw *et al.*, SMC note 97/17 (unpublished).
- [18] SMC Collaboration, B. Adeva *et al.*, ‘‘Polarized Double Cell Target of the SMC’’ (in preparation).
- [19] EMC Collaboration, J. Ashman *et al.*, Phys. Lett. B **206**, 364 (1988); Nucl. Phys. **B328**, 1 (1989).
- [20] V. W. Hughes and J. Kuti, Annu. Rev. Nucl. Part. Sci. **33**, 611 (1983); T. Pussieux and R. Windmolders, in *Internal Spin Structure of the Nucleon*, edited by V. W. Hughes and C. Cavata (World Scientific, Singapore, 1995), p. 212.
- [21] E143 Collaboration, K. Abe *et al.*, Phys. Rev. Lett. **76**, 587 (1996).
- [22] E. Rondio, J. Kiryluk, and A. Tripet, ‘‘Inclusive Asymmetry Calculation Using Events with Hadrons,’’ SMC note SMC/97/07 (unpublished).
- [23] A. Bravar, K. Kurek, and R. Windmolders Program POLDIS,

- Comput. Phys. Commun. **105**, 42 (1997).
- [24] NMC Collaboration, M. Arneodo *et al.*, Nucl. Phys. **B483**, 3 (1997).
- [25] SLAC Collaboration, L. Whitlow *et al.*, Phys. Lett. B **250**, 193 (1990).
- [26] V. N. Gribov and L. N. Lipatov, Sov. J. Nucl. Phys. **15**, 438 (1972); **15**, 675 (1972); G. Altarelli and G. Parisi, Nucl. Phys. **B126**, 298 (1977); Yu. L. Dokshitzer, Sov. Phys. JETP **46**, 641 (1977).
- [27] W. Buck and F. Gross, Phys. Rev. D **20**, 2361 (1979); M. Z. Zuilhof and J. A. Tjon, Phys. Rev. C **22**, 2369 (1980); M. Lacombe *et al.*, *ibid.* **21**, 861 (1980); R. Machleidt *et al.*, Phys. Rep. **149**, 1 (1987); A. Yu. Umnikov *et al.*, University of Alberta Report No. Alberta-Thy-29-94, 1994.
- [28] E. P. Sichtermann, Ph.D. thesis, Free University of Amsterdam, 1998.
- [29] E143 Collaboration, K. Abe *et al.*, Phys. Rev. Lett. **74**, 346 (1995); **75**, 25 (1995).
- [30] NMC Collaboration, M. Arneodo *et al.*, Nucl. Phys. **B487**, 3 (1997).
- [31] NMC Collaboration, P. Amaudruz *et al.*, Phys. Rev. Lett. **66**, 2712 (1991); NMC Collaboration, M. Arneodo *et al.*, Phys. Rev. D **50**, R1 (1994).
- [32] NA51 Collaboration, A. Baldit *et al.*, Phys. Lett. B **332**, 244 (1994).
- [33] E772 Collaboration, P. L. McGaughey *et al.*, Phys. Rev. Lett. **69**, 1726 (1992).
- [34] E866 Collaboration, E. A. Hawker *et al.*, Phys. Rev. Lett. **80**, 3715 (1998).
- [35] C. Bourrely *et al.*, Prog. Theor. Phys. **99**, 1017 (1998).
- [36] S. D. Bass and M. M. Brisudova, hep-ph/9711423.
- [37] BCDMS Collaboration, A. C. Benvenuti *et al.*, Phys. Lett. B **233**, 485 (1989).
- [38] E665 Collaboration, M. R. Adams *et al.*, Phys. Rev. D **54**, 3006 (1996).
- [39] SLAC Collaboration, L. W. Whitlow *et al.*, Phys. Lett. B **282**, 475 (1992).
- [40] H1 Collaboration, S. Aid *et al.*, Nucl. Phys. **B470**, 3 (1996).
- [41] ZEUS Collaboration, M. Derrick *et al.*, Z. Phys. C **72**, 399 (1996).
- [42] T. Çuhadar, Ph.D. thesis, Free University of Amsterdam, 1998.